

AD \_\_\_\_\_

Award Number: DAMD17-00-1-0465

TITLE: A Novel Method for Determining Calcification Composition

PRINCIPAL INVESTIGATOR: Andrew D. A. Maidment, Ph.D.

CONTRACTING ORGANIZATION: University of Pennsylvania  
Philadelphia, PA 19104

REPORT DATE: December 2005

TYPE OF REPORT: Final

PREPARED FOR: U.S. Army Medical Research and Materiel Command  
Fort Detrick, Maryland 21702-5012

DISTRIBUTION STATEMENT: Approved for Public Release;  
Distribution Unlimited

The views, opinions and/or findings contained in this report are those of the author(s) and should not be construed as an official Department of the Army position, policy or decision unless so designated by other documentation.

REPORT DOCUMENTATION PAGE				Form Approved OMB No. 0704-0188	
Public reporting burden for this collection of information is estimated to average 1 hour per response, including the time for reviewing instructions, searching existing data sources, gathering and maintaining the data needed, and completing and reviewing this collection of information. Send comments regarding this burden estimate or any other aspect of this collection of information, including suggestions for reducing this burden to Department of Defense, Washington Headquarters Services, Directorate for Information Operations and Reports (0704-0188), 1215 Jefferson Davis Highway, Suite 1204, Arlington, VA 22202-4302. Respondents should be aware that notwithstanding any other provision of law, no person shall be subject to any penalty for failing to comply with a collection of information if it does not display a currently valid OMB control number. PLEASE DO NOT RETURN YOUR FORM TO THE ABOVE ADDRESS.					
1. REPORT DATE 01-12-2005		2. REPORT TYPE Final		3. DATES COVERED 1 Jun 2000 – 30 Nov 2005	
4. TITLE AND SUBTITLE  A Novel Method for Determining Calcification Composition				5a. CONTRACT NUMBER	
				5b. GRANT NUMBER DAMD17-00-1-0465	
				5c. PROGRAM ELEMENT NUMBER	
6. AUTHOR(S)  Andrew D. A. Maidment, Ph.D.  Email: <a href="mailto:Andrew.Maidment@uphs.upenn.edu">Andrew.Maidment@uphs.upenn.edu</a>				5d. PROJECT NUMBER	
				5e. TASK NUMBER	
				5f. WORK UNIT NUMBER	
7. PERFORMING ORGANIZATION NAME(S) AND ADDRESS(ES)  University of Pennsylvania Philadelphia, PA 19104				8. PERFORMING ORGANIZATION REPORT NUMBER	
9. SPONSORING / MONITORING AGENCY NAME(S) AND ADDRESS(ES) U.S. Army Medical Research and Materiel Command Fort Detrick, Maryland 21702-5012				10. SPONSOR/MONITOR'S ACRONYM(S)	
				11. SPONSOR/MONITOR'S REPORT NUMBER(S)	
12. DISTRIBUTION / AVAILABILITY STATEMENT Approved for Public Release; Distribution Unlimited					
13. SUPPLEMENTARY NOTES Original contains colored plates: ALL DTIC reproductions will be in black and white.					
14. ABSTRACT Breast calcifications can be divided into two broad categories. Type I are composed of calcium oxylate, while type II calcifications all have some phosphorus content, most typically calcium hydroxyapatite. Type II calcifications are known to be associated with carcinoma, while it is generally accepted that the exclusive finding of type I calcifications is indicative of benign lesions. We have developed a technique that will determine the composition of calcifications based on x-ray coherent scatter (analogous to x-ray diffraction). In this grant, we have designed a dedicated coherent scatter imaging system. We have characterized the design and optimized the system. We have developed calibration methods and used these to identify the chemical composition of calcific materials ex vivo. We have also evaluated the potential to image materials in vivo. However, due to physical limitations, we believe that development of an in vivo system is unlikely. We believe that this methodology has the most value as a screen process in the histological evaluation of specimens.					
15. SUBJECT TERMS Breast Cancer, Mammography, X-ray Polarization					
16. SECURITY CLASSIFICATION OF:			17. LIMITATION OF ABSTRACT	18. NUMBER OF PAGES	19a. NAME OF RESPONSIBLE PERSON
a. REPORT	b. ABSTRACT	c. THIS PAGE			USAMRMC
U	U	U	UU	43	19b. TELEPHONE NUMBER (include area code)

## Table of Contents

Introduction.....	4
Body.....	5
Key Research Accomplishments.....	37
Reportable Outcomes.....	38
Conclusions.....	41
References.....	42
Appendices.....	43

## Introduction

Calcifications can be divided into two broad categories. Type I are composed of weddellite (calcium oxalate dihydrate) and whewellite (calcium oxalate monohydrate); by contrast, all type II calcifications have some phosphorus content, most typically calcium hydroxyapatite. Type II calcifications are known to be associated with carcinoma, while it is generally accepted that the exclusive finding of type I calcifications is indicative of benign lesions.

In this grant, we proposed to develop a technique that could determine the composition of calcifications prior to biopsy, thereby allowing one to avoid biopsy on Type I calcifications. We proposed that coherent scatter imaging (which is similar to x-ray diffraction imaging) might be able to determine the chemical composition of calcifications. In this grant, we specifically proposed to design a dedicated detector to measure coherent scatter, and to optimize image acquisition with this detector. This detector was built and is located in the X-ray Physics Laboratory of the University of Pennsylvania. We further proposed to characterize the detector, and characterize specific raw materials to determine a basis set for compositional analysis. This too was successful.

Finally, we proposed to validate this design by testing the scattering of calcifications located within surgical biopsy specimens, prior to histology. This last step proved problematic. The scatter signal that we recorded was small; it was only possible to identify calcific materials in very thin materials which simulated very thin tissue sections. While we were able to obtain signal from prepared materials, we never were able to obtain scatter signatures for biological specimens.

## **Body**

### **1. Statement of Work**

The work for this grant was divided into six tasks. They are outlined as follows:

#### **1.1. Task 1: Coherent Scatter Detector Development**

We first proposed to design and construct an appropriate detector. This would allow experiments to be performed to gather data for optimization (Tasks 2 and 3). The detector would be modified as necessary based on these results.

#### **1.2. Task 2: Computer Modeling of Coherent Scatter**

A model of the coherent scatter would be developed, based first on the assumption of a monoenergetic x-ray beam. The model would then be expanded to consider polyenergetic spectra to study effect of spectrum on scatter. In addition, the effects of pencil beam size, and finite object size would be studied. A method would be developed to separate the scatter data into basis sets. Finally, issues related to SNR and dose would be added to optimize detector design and operating conditions

#### **1.3. Task 3: Detector Characterization**

Characterize the detector in terms of imaging parameters. These data could then be used to optimize the detector design.

#### **1.4. Task 4: Phantom Studies – Basis Set Determination**

A series of experiments were proposed. First we proposed to characterize the detector in terms of basis materials, including linearity. We would develop a basis set of materials (calcifications, adipose, glandular, etc.), and characterize the detector in its ability to distinguish admixtures of materials. Finally, we would develop beam hardening and other corrections as needed to make system accurately report data that are linear in terms of the basis materials.

#### **1.5. Task 5: Specimen Study**

We proposed to recruit a group of patients scheduled for surgery on the basis of breast calcifications, and image the surgical specimens prior to histology. We would analyze these data and correlate pathology results with compositional analysis. It was not possible to complete this task, as the signal obtained from clinical specimens was too small.

#### **1.6. Task 6: *In Vivo* Imaging Feasibility Study Design**

Finally, we proposed to determine the feasibility of *in vivo* imaging, including dose, by using data derived in Task 5 to estimate the statistical properties of this test. The method currently appears to be infeasible *in vivo*, and hence this task was not completed.

## 2. Administrative Note

This grant was originally awarded when Dr. Maidment was on the faculty of Thomas Jefferson University. The work in this grant commenced on July 1, 2001. During that time, Dr. Andrew Maidment (PI) and Dr. Michael Albert (Research Associate) worked on the grant. Effective February 1<sup>st</sup>, 2003, Dr. Maidment resigned his position at Thomas Jefferson University and began working at the University of Pennsylvania.

The grant was transferred to the University of Pennsylvania, and was active from October 13, 2003 to May 31, 2006. During this time, Dr. Andrew Maidment, Dr. Michael Albert, and Dr. Harry Kao worked on the grant. Dr. Albert performed many of the initial experiments. He developed much of the initial ideas in the grant. Dr. Kao helped to perfect the work in the grant. He spent significant time performing careful experiments. He also adapted all of the data analysis methods, and made them robust. Dr. Maidment provided overall oversight of the grant and supervised the data analysis.

The combination of moving the laboratory to the University of Pennsylvania; designing, building and moving into new laboratory space; obtaining appropriate equipment; and selecting appropriate people took some time, and significantly delayed the grant from its original time line. At the end of the grant period, first Dr. Albert and then Dr. Kao resigned from the University of Pennsylvania. As a result, the final report for the grant was further delayed.

## 3. Imaging System Development

An imaging system has been built for performing coherent scatter and small angle x-ray diffraction experiments. The system is shown schematically and graphically in Figure 1. The system consists of an x-ray tube, added filtration to shape the x-ray spectrum, a series of three collimators ( $S_1$ ,  $S_2$ , and  $S_3$ ), a sample stage, an x-ray image intensifier (XRII) and a CCD camera (not shown). The system is based on a scanning pencil beam. The x-ray beam is filtered (M), and collimated ( $S_1$ ) before hitting the target (X). The primary x-ray beam is attenuated by a beam stop (B). The radial distribution of the scattered x-rays is recorded on the detector (F).

X-ray Spectra: The x-ray tube has a molybdenum target. Typically, the tube is operated in conjunction with 25  $\mu\text{m}$  or 50  $\mu\text{m}$  Niobium added filtration. This serves to eliminate the molybdenum K- $\beta$  radiation, producing an essentially monochromatic x-ray beam at the K- $\alpha$  line of molybdenum (17.4 keV). The x-ray spectra are described in more detail later in this report.

The system is enclosed in a lead-lined box, and is compliant with Pennsylvania state regulations for cabinet x-ray units (the box is not shown in the image). A new (refurbished) x-ray generator (General Electric Medical Systems, Model 500T, Milwaukee, WI) was installed for the imaging system when it was moved to the University of Pennsylvania. The new x-ray generator/x-ray tube combination allows exposures of up to 49 kVp and 800 mAs. Greater counting statistics can be obtained by averaging multiple images.

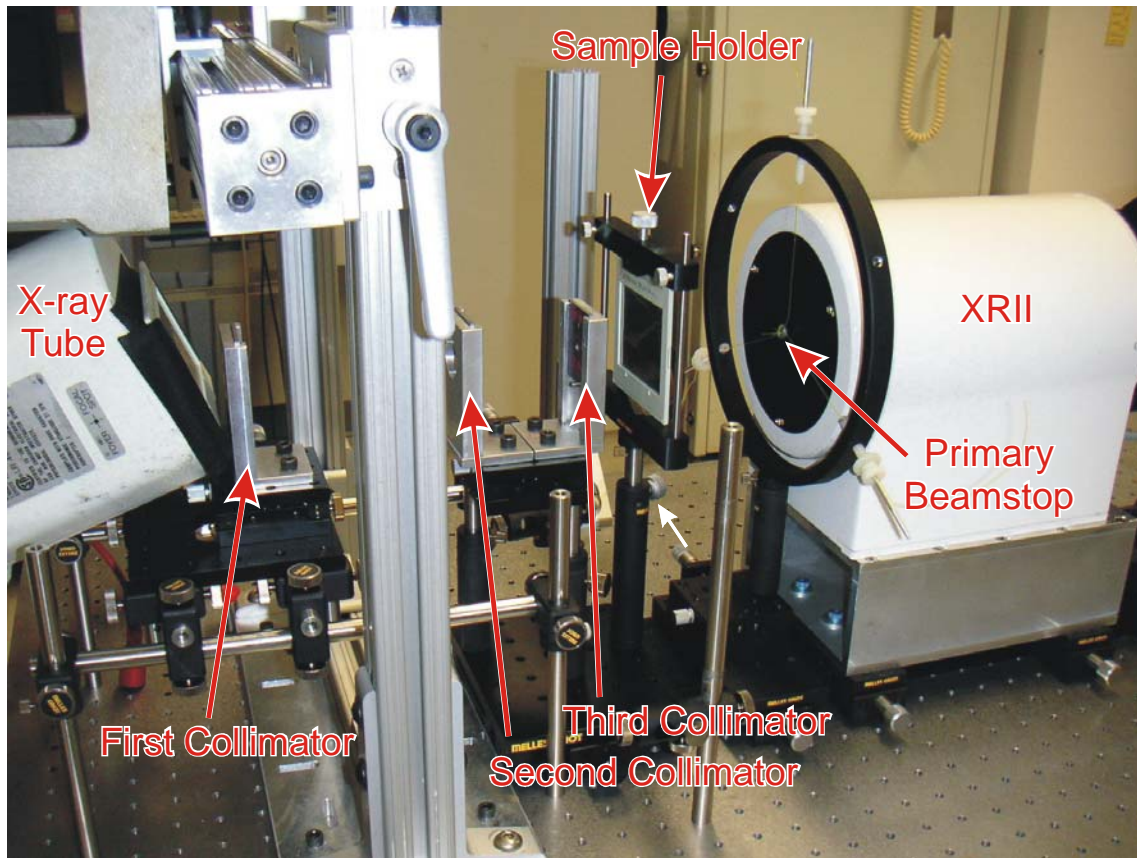
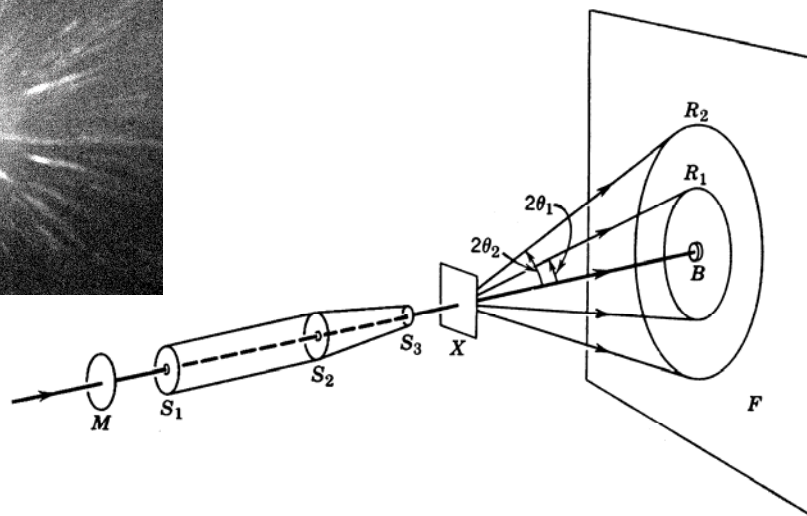
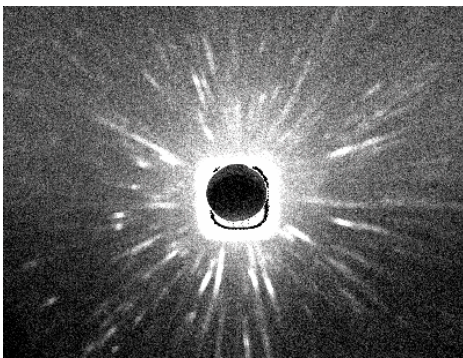


**Figure 1:** Picture of the imaging system (above). The system consists of an x-ray source, collimators, a sample holder, and an x-ray image intensifier (XRII) and CCD camera. The imaging system is shown in schematic below. The x-ray beam is filtered ( $M$ ) and collimated ( $S_1, S_2, S_3$ ) before being incident on the sample ( $X$ ). The diffracted beam forms rings on the detector ( $F$ ). Failure to include the 3<sup>rd</sup> collimator results in significant scatter from the prior collimators being recorded (see inset image).



The x-ray unit was modified to allow computer control using an Ontrak ADU218 USB Relay Interface (Ontrak Control Solutions, Sudbury, ON, Canada) and an Icron Ranger Model 422 USB extender (Icron, Vancouver, BC, Canada). Dedicated realtime software was written to control the x-ray generator and computer.

**Collimators:** The three collimators serve to form a small spot of radiation that is used to generate the scattered image. We have learned that it is necessary to have 3 collimators in the beam. Collimators  $S_1$  and  $S_2$  define the size and solid angle of the beam. Collimator  $S_3$  removes any coherent scatter generated by collimator  $S_2$ . Without collimator  $S_3$ , the upstream collimators will produce more coherent scatter than the samples we have been examining. An image of the coherent scatter observed in the absence of collimator  $S_3$  is shown in Figure 1 (inset). A set of interchangeable x-ray collimators has been built and tested, and has been incorporated into the test device. The collimator set allows pencil beams of different diameter to be used. We typically use a pencil beam of 1.0 mm diameter, but have built collimators of 0.5, 0.75, 1.0, 1.5 and 2.0 mm to test the effect of other beam sizes.

**Detector:** The x-ray image intensifier (Model E5881J-P1, Toshiba Electron Tubes and Devices, Tokyo, Japan) and CCD camera (Dalsa 1M30, Waterloo, Ontario, Canada) were chosen after initial experiments were performed on a series of test devices. The intensifier has a 4" open diameter, and high intrinsic spatial resolution (7.1 lp/mm) and conversion efficiency. A lead blocker is placed on the front of the image intensifier to prevent the primary x-ray beam from striking the XRII. The output of the image intensifier is recorded with a CCD camera using a 75 mm – 50 mm relay lens pair. Custom software was developed to acquire images. This software integrated the operation of the CCD camera with the operation of the x-ray generator.

### Mass Attenuation Coefficients for Soft Tissue

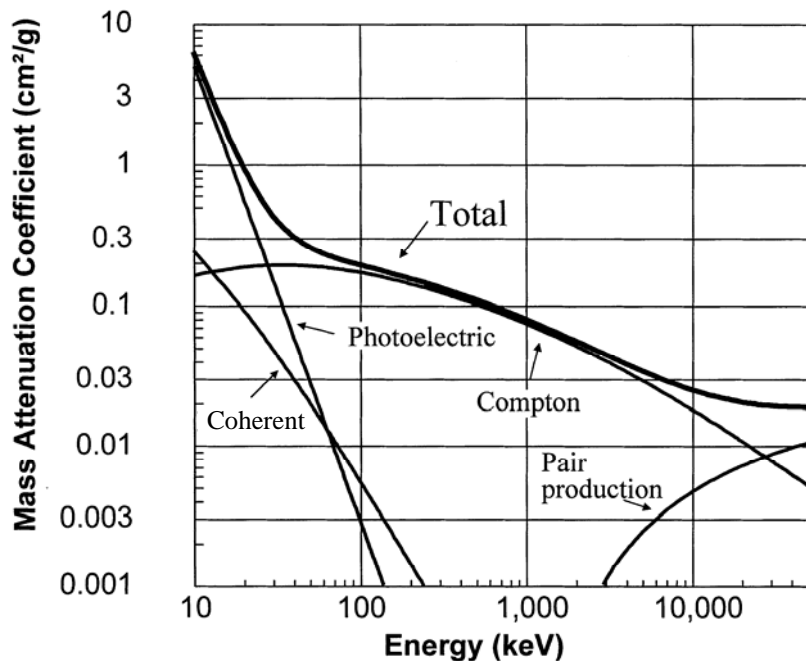


**Figure 2: Energy dependence of x-ray interaction coefficients for soft tissue. The probability of coherent scatter decreases quadratically with energy**

## 4. X-ray Spectra

Coherent scattering is energy dependent; the probability of coherent scatter decreases quadratically with increasing x-ray energy. In addition, the angle of the scatter decreases with increasing x-ray energy. The energy dependence of coherent scatter of soft tissue is shown in Figure 2 (note, this figure is integrated over all angles and ignores certain form factor details). As a result, lower energies will result in increased coherent scatter. However, the practical low-energy limit is determined by patient dose. As such, we opted to use a relative low energy, pseudo-monoenergetic x-ray beam.

In opting for this method of producing an x-ray spectrum, we are limited to the target materials available, namely molybdenum, rhodium and tungsten. We selected molybdenum, based on its energy spectrum and its availability. Rhodium target x-ray tubes must be operated at a lower mA, and require a high-speed rotor; tungsten characteristic energies are too high. Thus, we produced x-ray spectra using a molybdenum (Mo) x-ray target material and niobium (Nb) filtration. The niobium will remove the Mo K- $\beta$  radiation. Niobium has a k-shell energy of 18.986 keV, which is between the K $\alpha$  (K $\alpha$ 1 = 17.4793 keV and K $\alpha$ 2 = 17.3743 keV) and K $\beta$  (19.6083 keV) energies of molybdenum. The result is that the K $\beta$  x-ray beam is more highly attenuated than the K $\alpha$ . Thus, a nearly mono-energetic x-ray beam can be produced.

The dependence between x-ray energy and patient dose is illustrated in Figure 3. Shown is the thickness of tissue that results in an 8-fold reduction of the intensity of the x-ray beam; equivalently, this thickness of tissue will result in 87% of the beam energy being absorbed in the breast tissue. At the proposed beam energy of 17.4 keV, this corresponds to a tissue thickness of 2 cm.

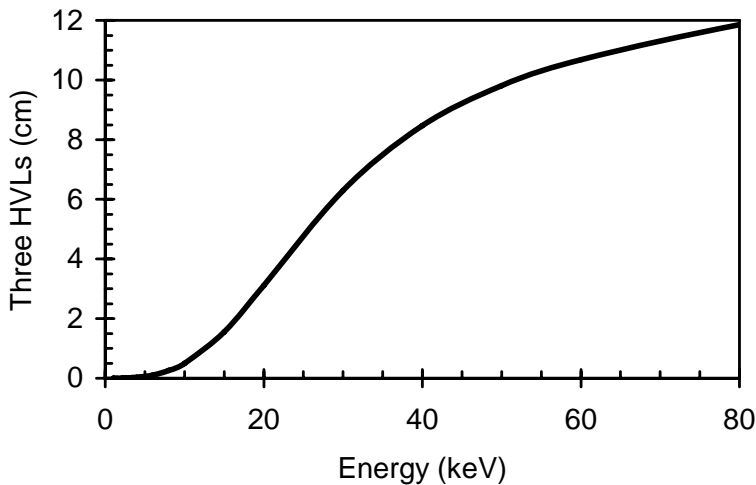


**Figure 3: The attenuation of breast tissue as a function of monoenergetic beam energy, shown in terms of half value layer thickness.**

The amount of niobium filtration was determined experimentally. The optimal filtration was a trade-off between energy resolution and fluence. In figure 4, we show the x-ray spectra achieved with various amounts of Mo and Nb filtration. The energy resolution

and relative fluence are given in Table 1. We most typically operated with 50  $\mu\text{m}$  of Nb filtration.

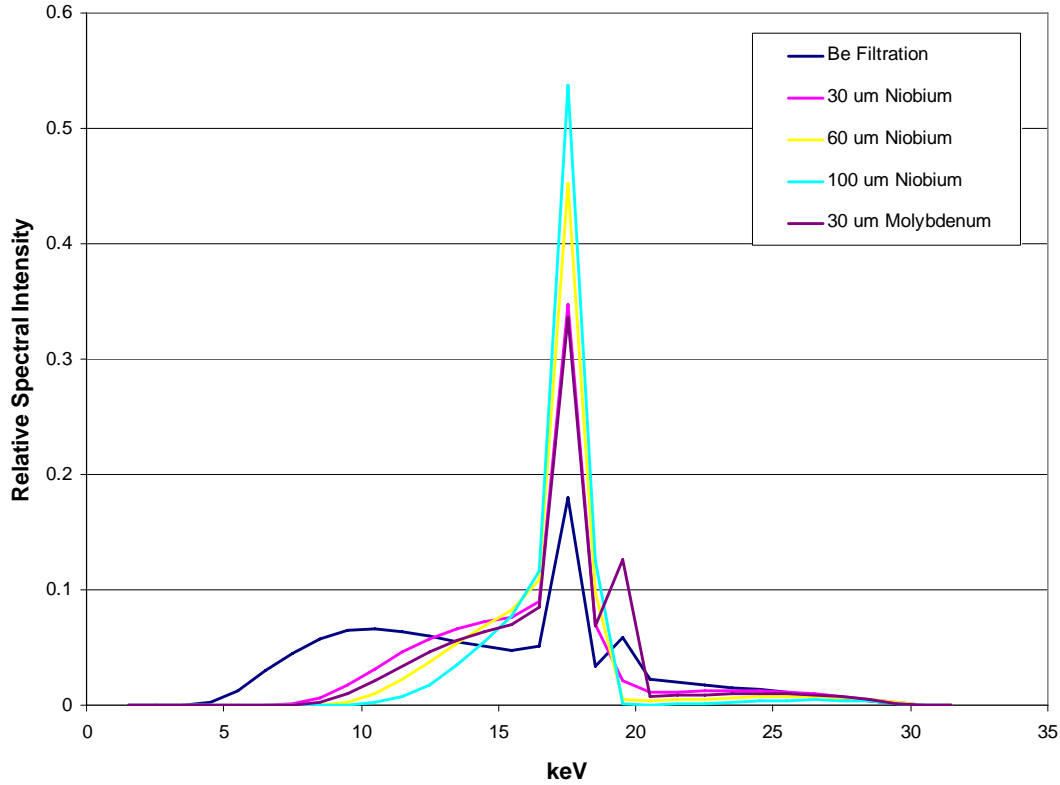


**Figure 4: Molybdenum-target x-ray spectra with various elemental filtration.** The spectra are normalized to unit area, and are calculated for a peak energy of 30 kV. The intrinsic spectrum of the x-ray tube is given by the beryllium (Be) filtration. A typical mammographic x-ray spectrum is 30  $\mu\text{m}$  of Mo. The Nb filtration is relatively effective at suppressing the Mo  $K_{\beta}$  characteristic radiation at  $\sim 20$  keV.

Niobium (um)	% k-alpha	Relative Fluence
0	26%	100.0%
30	51%	33.6%
45	59%	23.2%
60	66%	16.8%
80	73%	11.4%
100	78%	8.0%
150	86%	3.5%
200	91%	1.6%
300	96%	0.4%

**Table1: The energy resolution (expressed as the percentage of the x-ray beam intensity given by the  $K_{\alpha}$  characteristic radiation), and the relative fluence of various amounts of niobium filtration.**

We verified the x-ray spectra calculations by performing x-ray diffraction experiments on the various x-ray beams. A Silicon wafer 1 mm thick, with a  $\langle 111 \rangle$  crystal orientation (Cemat Silicon SA, Warsaw, Poland) was placed in the x-ray beam such that the Bragg angle corresponded approximately to that expected of Mo  $K_{\alpha}$  radiation. Silicon will

reflect the Mo  $K\alpha$  radiation at a Bragg angle of  $\sim 45^\circ$  (reflected beam is emitted at  $90^\circ$ ) on the 11 11 11 plane of the crystal. A sample image of the reflected x-ray beam is shown in Figure 5. The image shows a series of lines corresponding to the reflected  $K\alpha$  and  $K\beta$  characteristic radiation lines; double lines correspond to the  $K\alpha_1$  and  $K\alpha_2$  radiation, single lines to the  $K\beta$ . The addition of a niobium filter has the effect of preferentially removing the  $K\beta$  radiation.

## Spectra with various filters

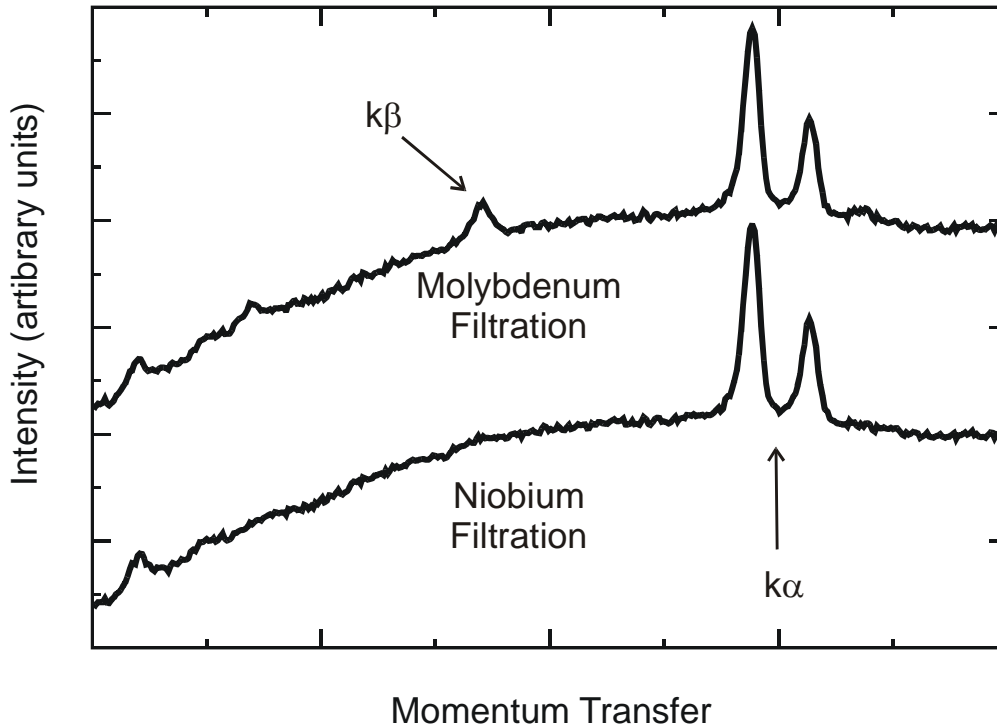


**Figure 5:** The intensity of x-ray beam as a function of momentum transfer (i.e., scatter angle measured by position on the x-ray detector). The two graphs differ by the beam filtration. Molybdenum filtration allows the  $k\beta$  radiation to be imaged, the niobium filtration not. Note that the  $k\beta$  lines are missing in the one graph. The two graphs are displaced for illustrative purposes only.

## 5. Imaging System Calibration

It was necessary to calibrate the imaging system in terms of scattering angle; i.e., it was necessary to map the spatial domain of the scatter images into diffraction angle ( $2\theta$ , Figure 1 bottom). Calibration was performed by obtaining diffraction patterns of known materials. Images were typically acquired by running the tube at 35 kVp, 100 mA, for 6 second intervals. Multiple images were acquired and averaged to improve image statistics.

Background intensity was measured without any material in the beam. This was used for subtraction from data acquired with materials in place. All acquired data were then plotted as a function of distance on the image intensifier (in terms of pixels) away from

the position of the primary beam, as determined without the beam stop. Using these plots, the background was scaled appropriately and then subtracted from the data for each of the materials. (The data analysis algorithm is discussed in more detail below)

The known positions of the first rhodium diffraction peaks were used to estimate the geometric factors need to scale distances in pixels into degrees. These data indicated that some effort was required to compensate for geometric distortions due to the curved surface of the image intensifier and distortions related to the electron optics.

The diffraction spectra of all of the materials investigated were calculated using Fhkl (Version 1.2 – 1994; <http://www.lmcp.jussieu.fr/sincris/logiciel/Fhkl/>). As input, we used data from “webelements” (<http://www.webmineral.com/>), the "MINCRYST" database (<http://database.iem.ac.ru/mincryst>) and the AMS database (<http://www.geo.arizona.edu/AMS>). These spectra were used to calibrate the imaging system using rhodium and molybdenum, and were also used to assess this calibration using hydroxyapatite, whewellite and weddellite (discussed below).

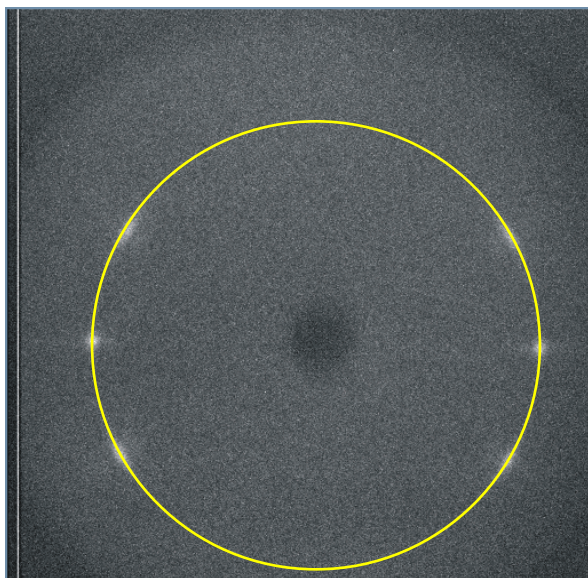


**Figure 6: A diffraction image of 25  $\mu\text{m}$  rhodium foil is shown. The primary diffraction of the rhodium is seen as 6 spots. At 17.4 keV, the scattering angle is 17°. The data was integrated radially to calculate the diffraction spectra shown in Figure 7.**

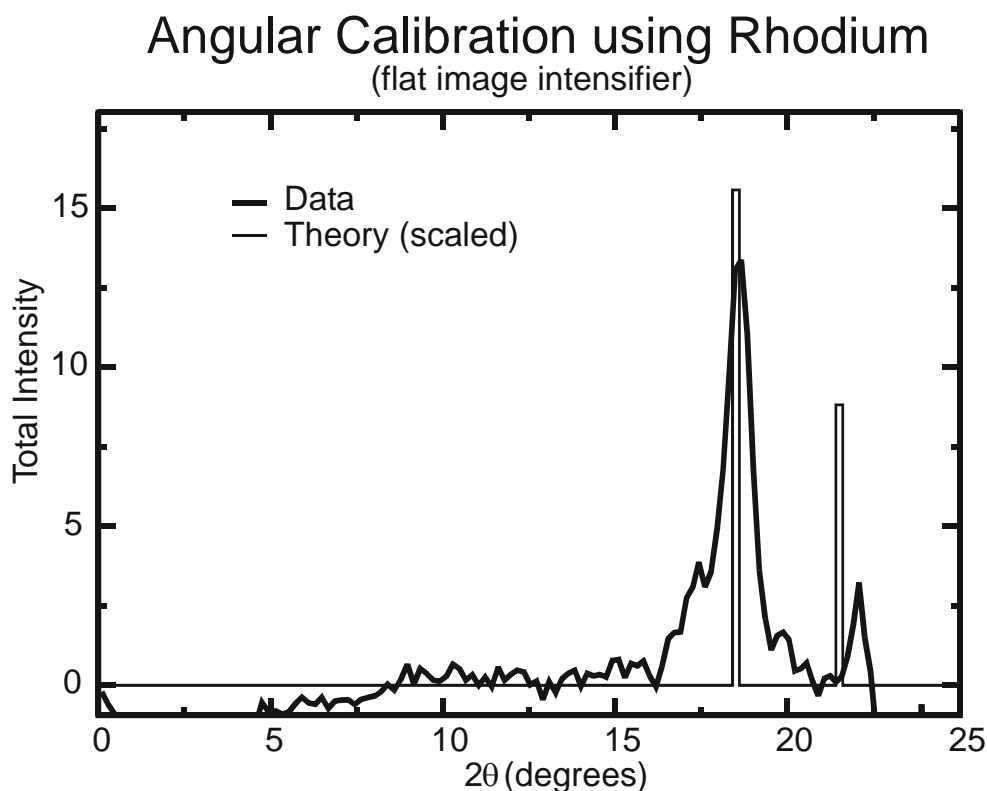


**Figure 7: Diffraction spectra of rhodium.** The measured diffraction spectrum (bold) is shown as compared to theory. The peak intensity of the spectra is arbitrary. The measured spectrum is shown linearly scaled as a function of angle to match the primary diffraction peak.

## 6. Calcification Synthesis

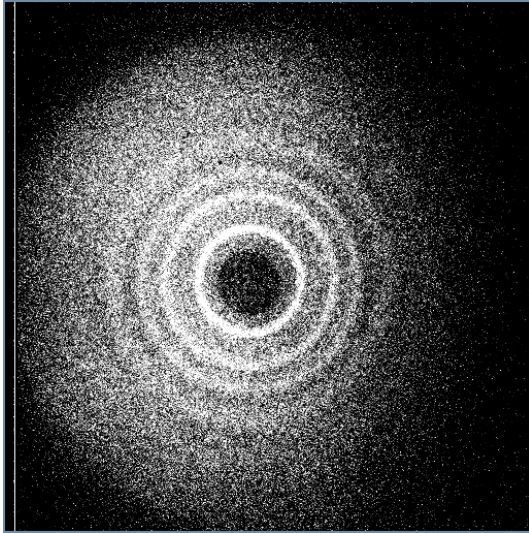
We have tested the imaging system using three types of calcium crystals. Two of the materials, hydroxyapatite (Alfa Aesar, Ward Hill, MA) and whewellite (Alpha Aesar), were obtained commercially. Weddellite was not commercially available; therefore, we chemically prepared our own weddellite.

We followed two papers on producing weddellite.<sup>1,2</sup> Precipitation is performed in distilled water at a pH of 10. The pH is set using a 0.01N NaOH solution. All chemicals are reagent grade. 1.2 liters of the  $\text{CaCl}_2$  solution is prepared at approximately 0.4 molar. To this is added 10 grams of  $\text{Na}_2\text{C}_2\text{O}_4$  dissolved in approximately 350 ml of water, again at pH 10. The sodium oxalate solution is added to the calcium chloride solution dropwise. The resulting calcium oxalate precipitates in very fine particles that require about a day to precipitate. We then remove the supernatant liquid, and wash the crystals by resuspending them several times in distilled water.

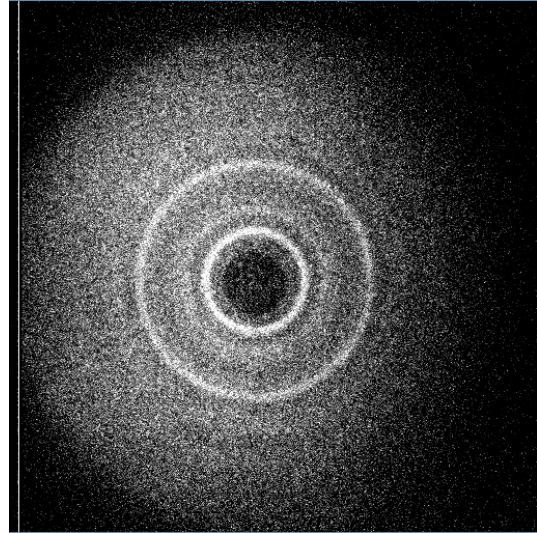
Evaluating of scattering of the reagent materials was performed in thin plate-like blocks. The reagents were suspended in an aqueous slurry in a large glass Petri dish, in which we had placed thin plastic sheets (typically 1 mil). The slurry was then allowed to dry. Typically a uniform layer of material would be formed on the plastic sheets. After the material had dried, the sheets would be removed and a small area in the center (typically 6 to 10 mm diameter) would be isolated by chipping the remaining materials away. Two precision thickness gauges would be placed on either side of the remaining material and a sharp straight-edged knife would be drawn back and forward across the material until it was flat and of accurate thickness. These are hereafter called “samples”

The areal density of each sample was measured. The area of the sample was determined by photographing each sample with a digital camera equipped with a macroscopic lens. The photograph would also contain a precise ruler. The surface area of the sample would be calculated by segmentation of the area using a thresholding algorithm. The tare mass of the sample would then be measured using a precision digital balance (the mass of each plastic sheet was measured prior to settling the slurry).

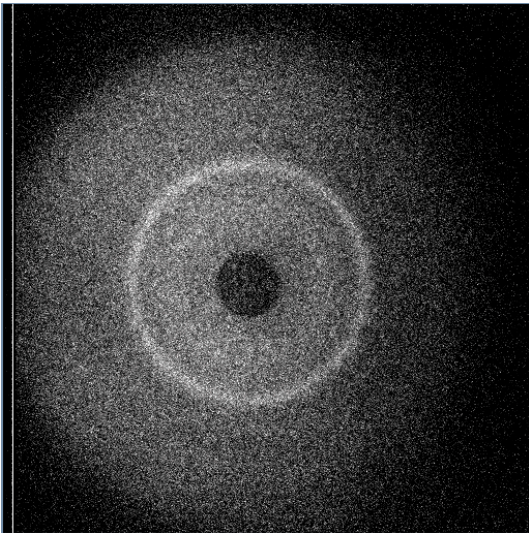
The scatter images of the three calcific materials are shown in Figure 8. As can be seen by comparing the spectra of the three materials, each can be easily distinguished from the other based upon the diffraction spectra. This is perhaps the single most important finding; it means that it is possible to distinguish breast calcifications based upon their composition using x-ray diffraction.



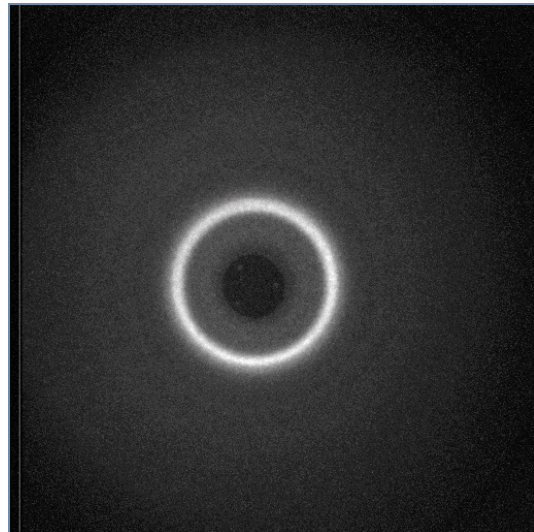
Whewellite



Weddellite



Hydroxyapatite



Wax

**Figure 8: Images obtained with the imaging system shown in Figure 1, for a variety of materials, as labeled. The diffraction spectra derived from these images are given in Figures 3-5.**

## 7. Image Processing

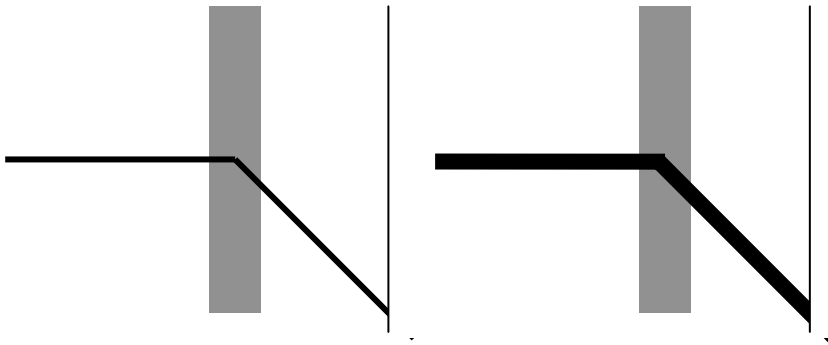
As demonstrated in Figure 6 and 8, the scatter patterns are radially symmetric. As a result, images were averaged radially to improve statistics.

Image processing began by acquiring a “background” spectra with only the plastic support material in the beam. (Note, in some instances, we produced spectra without the support material and in those instances, the background spectra were acquired without any material in the beam). These background spectra still resulted in coherent scattering from the plastic support and the air. Multiple spectra would be acquired and averaged to reduce the background variations.

A material spectrum would be acquired next. The averaged background spectra image would then be subtracted from the material spectra. The difference spectrum would then be averaged radially about the center of the x-ray beam. The center of the beam was determined in a separate experiment in which a low intensity primary image was acquired while the beam stop was removed. The average was calculated per unit radial angle, and hence a compensation for increasing annular area (as a function of increasing radial angle) was applied. All spectra shown hereafter have been processed in this way

## 8. Determination of Optimal Beam Diameter

Numerous experiments were conducted to understand the impact of various design features on the spectra being measured. The diameter of the interrogating pencil beam determines both the x-ray fluence on the sample (and hence detector), and the blurring of the spectra; this latter effect is illustrated in Figure 9.



**Figure 9: The effect of pencil beam diameter. The pencil beam is shown incident upon the specimen, and a single scattering angle is illustrated. The width of the beam at the detector is determined both by the incident beam diameter and the scattering angle.**

We experimentally determined our preferred beam diameter by measuring the diffraction spectra using various collimator pinholes in collimators  $S_1$  and  $S_2$  (see Figure 1). Spectra for various collimator sizes are shown in Figure 10. The spectra have been normalized to 1 at the peak of the primary scattering angle for calcium hydroxyapatite. Based on these measurements, we deemed the 1 mm diameter pencil beam to be optimal. This diameter allowed a good compromise between angular resolution and image

statistics. Angular resolution was determined at the full-width at 85% of the peak value. This was chosen based on the shape of the scattering spectra for large collimator diameters (note that the peak below the primary peak is blurred for large diameters).

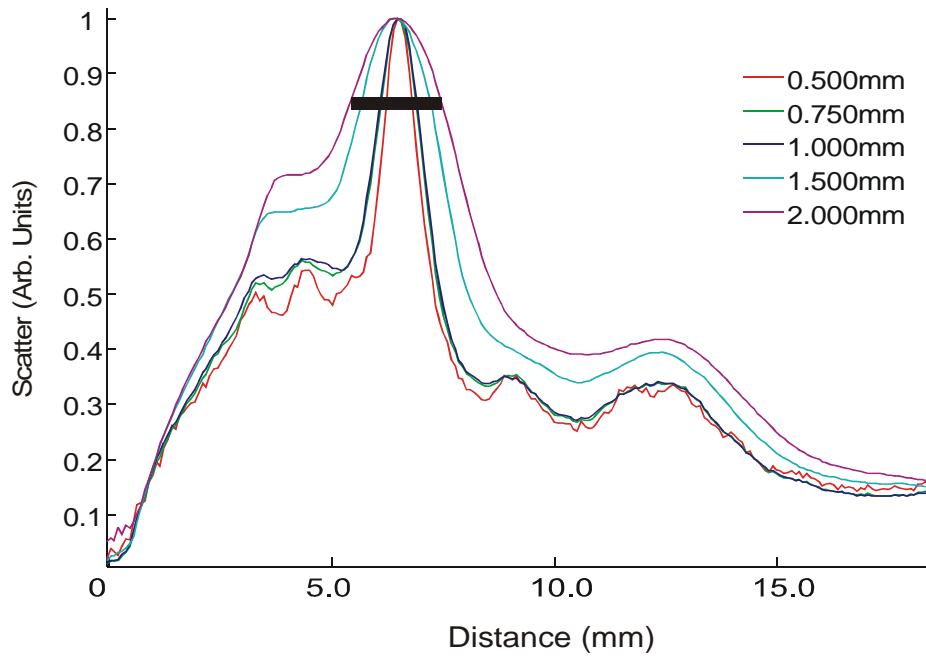


**Figure 10:** The scatter profile of calcium hydroxyapatite is shown as a function of beam diameter. The diameter of the pencil beam was varied by altering the diameter of the  $S_1$  and  $S_2$  collimators. The use of larger diameters resulted in smoother spectra; reducing statistical fluctuations, but as reducing the spectral detail.

## 9. Determinants of Scatter Intensity

The intensity of the scatter recorded on the detector is determined by the x-ray energy, the calcification thickness, and the thickness of the tissue sample. The effect of the latter two factors is detailed here.

### 9.1. Effect of Calcification Thickness

The thickness of the calcification will affect the scattered signal in two ways. First, the thicker the calcification, the greater the probability that an x-ray will be scattered in a given direction. Secondly, the thicker the calcification, the longer the path of the x-rays that pass through the calcification, thus reducing the intensity of the scattered beam. The path length will increase as the angle increases.

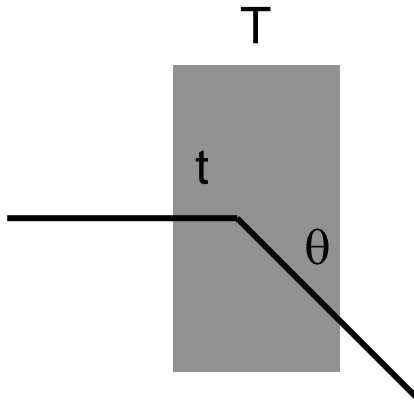


**Figure 11: A schematic view of the scatter of x-rays by a thick target.**

The scatter,  $S$ , of x-rays from a thick target is determined by the fluence incident upon the target,  $\Phi$ , the area of the irradiating x-ray beam,  $A$ , the probability of scatter occurring ( $\sigma$ ) at a specific angle,  $\theta$ , and the attenuation of the x-rays along the path. The last term must be calculated for all scattering points ( $t$ ) through the thickness ( $T$ ) of the target. The scatter can thus be calculated as

$$S = \Phi A \int_0^T \sigma \exp\left(-\frac{\mu t}{\rho}\right) \exp\left(\frac{-\mu(T-t)}{\rho \cos(2\theta)}\right) dt$$

$$= \frac{\Phi A \sigma}{\left(\frac{\mu}{\rho}\right) \left(\frac{1}{\cos(2\theta)} - 1\right)} \left( \exp\left(-\frac{\mu T}{\rho}\right) - \exp\left(\frac{-\mu T}{\rho \cos(2\theta)}\right) \right)$$

where  $\mu/\rho$  is mass attenuation coefficient at the calcific material.

We have performed a series of experiments measuring the scatter intensity as a function of calcific target thickness. The targets were prepared using the method described in Section 6. The signal was determine by integrating the signal under each major peak (the limits of integration being determined by the full-width half-max of the peak). This integration was performed for each major peak. Next, a multiple parameter fitting

algorithm was applied to fit the scattered signal of the various peaks against the measured intensities.

In total, 13 different thicknesses of calcium hydroxyapatite were tested, varying from  $0.0418 \text{ gm/cm}^2$  to  $0.213 \text{ gm/cm}^2$ . The imaging system was aligned so as to allow the peaks at  $14.75^\circ$  and  $21.6^\circ$  to be visualized. The intensities of the two peaks were simultaneously fit in terms of the scatter cross-section  $\sigma$  at each angle, and a global offset to the data. The outcome of the fitting procedure is shown in Figure 12. The upper (blue) data and fit correspond to the peak at  $14.75^\circ$  and the lower (red) data and fit correspond to the peak at  $21.6^\circ$ . The RMS error in the fit is 1.45. A similar fit on the first two peaks of whewellite resulted in a RMS error of 2.75 for 9 samples spanning the range of  $0.080 \text{ gm/cm}^2$  to  $0.517 \text{ gm/cm}^2$ .

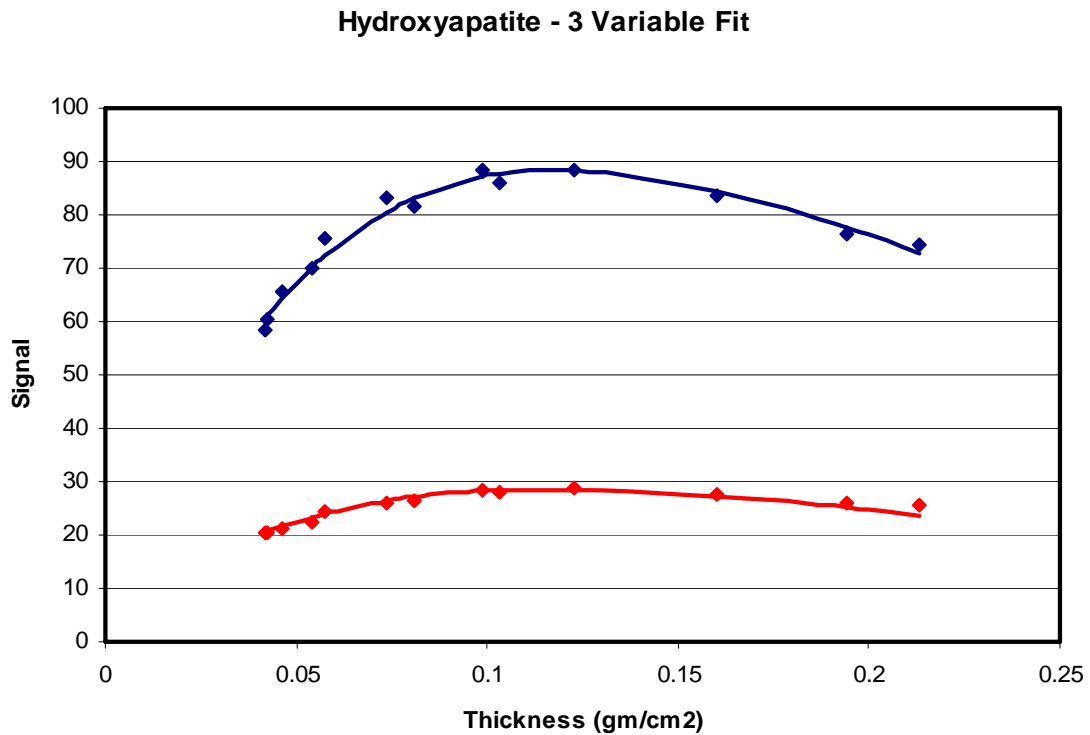


**Figure 12:** Experimental (points) and calculated (lines) values of scatter as a function of sample thickness. The scatter in two peaks are shown; blue corresponds to the scatter peak at  $14.75^\circ$  and red corresponds to the peak at  $21.6^\circ$ . The RMS error in the fit is 1.45. The signal is expressed in arbitrary units.

## 9.2. Effect of Tissue Thickness

The signal recorded by the detector is also determined by the amount of other materials in the x-ray beam. Consider the situation illustrated in Figure 13. A given point in the detector, P, will record scatter from many locations within the sample, including both soft tissue (grey), and calcification (black). It is not possible to determine the source of the scatter in this geometry. The material above the calcification (as drawn) will have the effect of reducing the intensity of the incident beam. The material below the calcification (as drawn) will reduce the intensity of the scattered beam.

It should also be noted that the location of the calcification within the soft tissue will be of some consequence. If the calcification is located proximal to the x-ray tube (top of the gray block as drawn), then the total path length of the incident and scattered x-ray will be greater than if the calcification were located proximal to the detector (bottom of the gray block). Due to the exponential nature of x-ray attenuation, the scattered x-ray signal will be lower if the calcification is located proximal to the x-ray tube than if proximal to the x-ray detector.

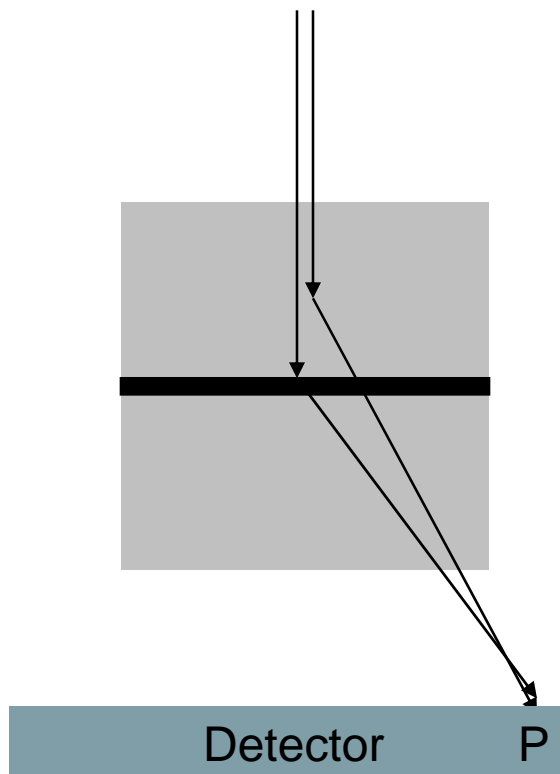


**Figure 13: The recorded scatter profiles will include the scatter from both the soft tissue (light gray) and calcific material (black). The overlying soft tissue will attenuate the x-ray beam prior to it striking the calcific material, while the underlying soft tissue will attenuate the scattered x-rays**

We have experimentally simulated the effect of soft-tissue above and below the calcification by adding breast-equivalent plastics to the x-ray beam. We experimented with different composition breast equivalent plastics from 100% adipose to 100% glandular(CIRS, Durham, NC). We also experimented with the placement of the plastic (whether proximal to the detector, the x-ray source, or equally split on both sides of the calcification).

The results of one such set of experiments are shown in Figure 14. In this experiment, the calcific material was located between two block of 50/50 breast equivalent plastic. The total thickness of the plastic was varied from zero to three centimeters in 1 cm steps. The actual plastic thickness was equally split above and below the calcification. For example, in the case of 1cm of plastic, 0.5cm was located between the x-ray source and the calcification, and 0.5 cm was located between the calcification and the detector. As can be seen from the figure, the calcification scatter profile (labeled “Baseline”) has multiple peaks, the largest at about 15° (the material is calcium hydroxyapatite). In comparison, the tissue-equivalent plastic has a single peak at low angles (NB: in the geometry being used, it is not possible to measure small angle scatter due to the lead beam-stop).

The scatter from the plastic dwarfs the scatter from the calcification. Although the hydroxyapatite peak is visible with 1cm of tissue-equivalent plastic, it is unlikely that we could recover this information accurately. This situation is even worse for greater thicknesses of breast equivalent material.

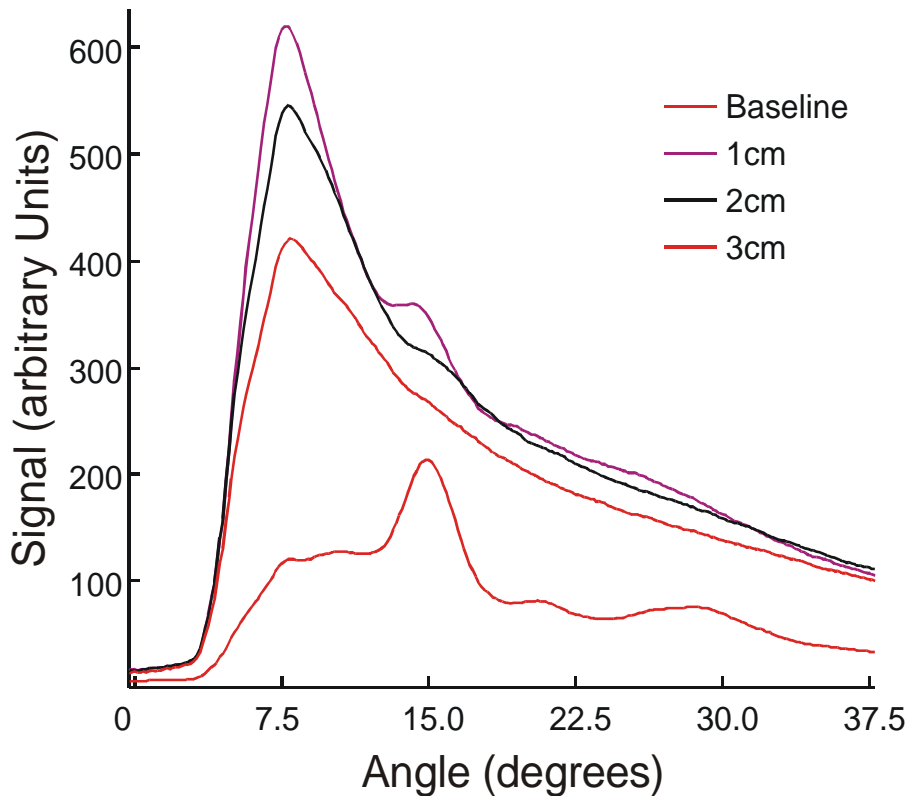


**Figure 14: Scatter profiles for calcific material (calcium hydroxyapatite), alone (“Baseline”) and embedded in tissue-equivalent plastic varying from 1 to 3 cm thick.**

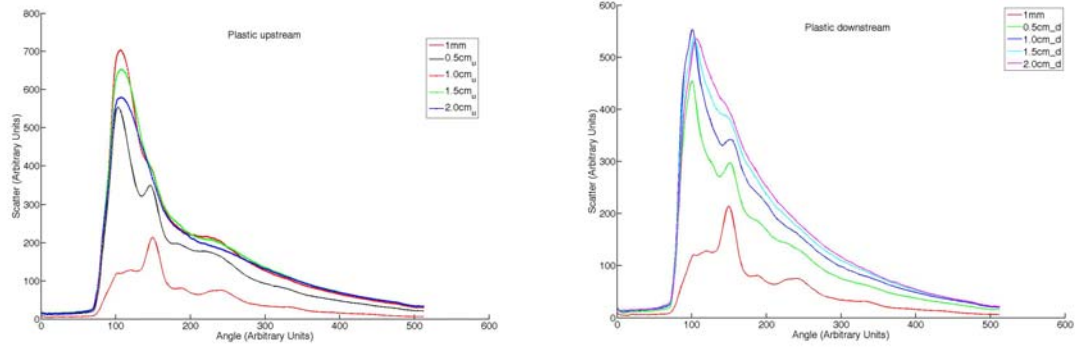


**Figure 15: Scatter profiles for plastic upstream (proximal to x-ray tube) and downstream (proximal to detector) of the calcific material.**

In figure 15, we consider the effect of the location of the calcific material within the tissue equivalent block. It is relevant to note that the calcific scatter signature is better preserved when the plastic is downstream (i.e., proximal to the detector). This is due to the fact that positioning the calcific material as close to the x-ray tube as possible results in a greater scatter signal from the calcification than from the other materials in the x-ray beam.

## 10. Diffraction Spectra of Reagents.

Up to this point, we have only discussed the spectra generated from the various calcific materials in generalities. However, a specific aim of the grant was to develop a method for identifying individual materials. We originally proposed to use the method of Cunningham *et al.* (3-5) to develop basis-sets from which we could sum individual components to form the measured scatter profiles. However, in the performance of this grant, we have realized that that method is not suitable to our task. The Cunningham method assumes that relatively equal contributions of the component materials exist. However, we end up having one of a few small calcification types being present in a block of soft tissue. As discussed above, the scatter from the soft-tissue far exceeds the scatter from the calcific materials (due almost entirely to the difference in volumes of the materials – especially since the calcific materials produce greater amounts of coherent scatter). Thus, we instead, have strived to understand the relative intensity of the scattered signal, with the expectation and understanding that distinguishing the materials can be achieved by identifying the ring patterns of the materials.

Diffraction images of calcium hydroxyapatite and calcium oxalate monohydrate are shown in Figure 16. The calculated spectra, measured spectra, and a calculated spectra blurred by a convolution kernel are shown in Figures 17 and 18. The measured spectra are compared in Figure 19.

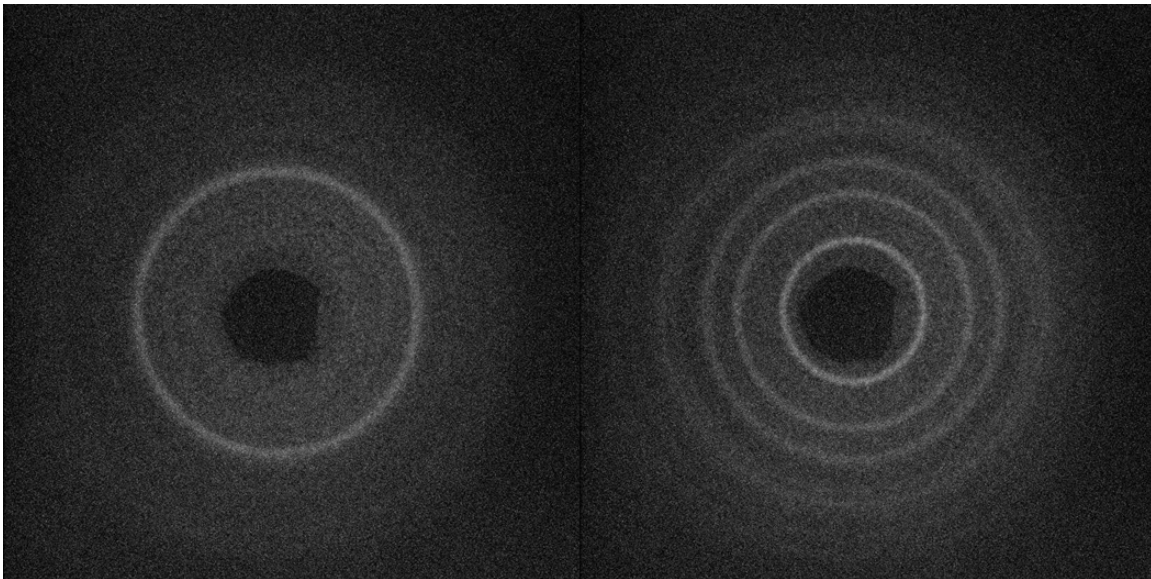


**Figure 16: Diffraction images of calcium hydroxyapatite (left), and calcium oxalate monohydrate (whewellite).**

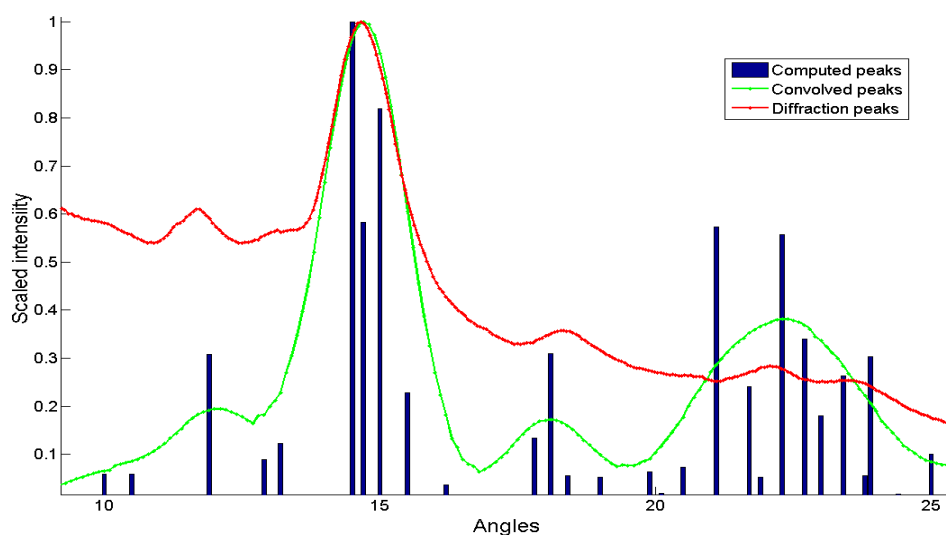


**Figure 17: Diffraction spectra of calcium hydroxyapatite. Shown at the calculated spectra (blue), theoretical spectra convolved by a blurring function (green), and measured diffraction spectrum (red)**

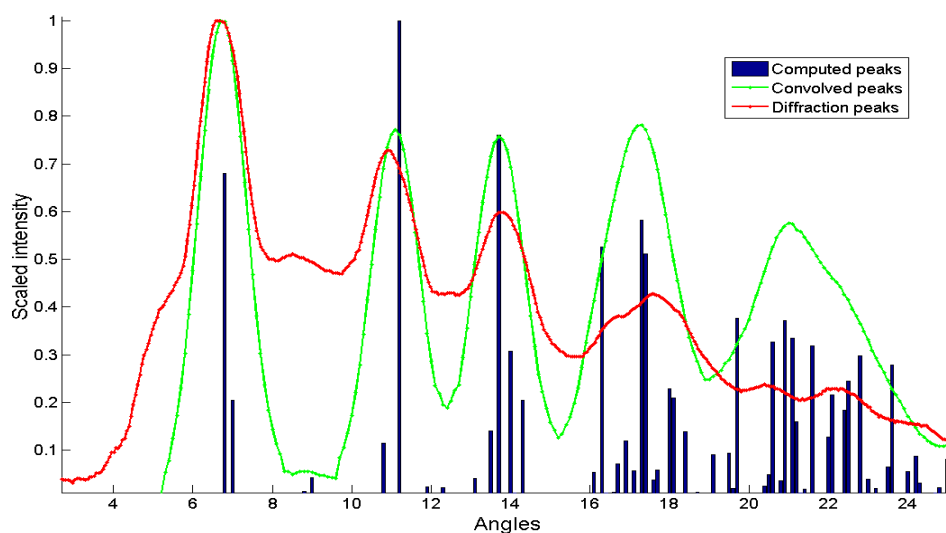


**Figure 18: Diffraction spectra of calcium oxalate monohydrate (whewellite). Shown at the calculated spectra (blue), theoretical spectra convolved by a blurring function (green), and measured diffraction spectrum (red)**

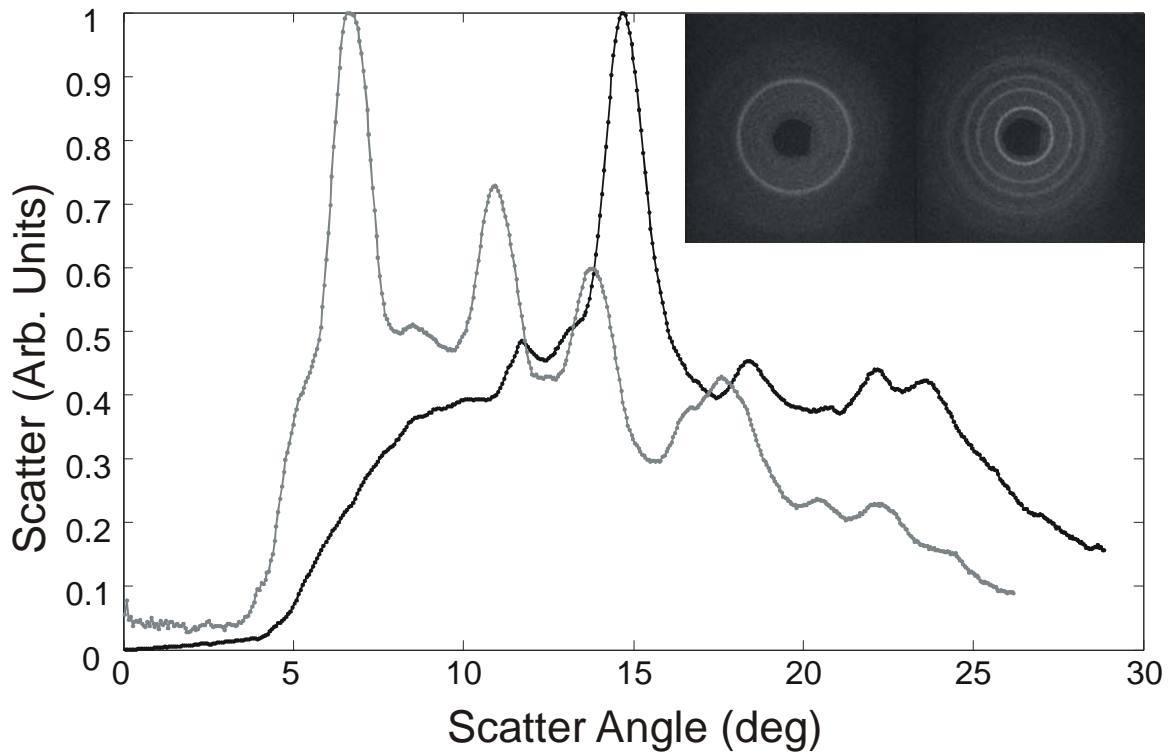


**Figure 19: Diffraction spectra of calcium hydroxyapatite (black) and calcium oxalate monohydrate (light gray) are compared.**

It is clear from these data that we can relatively accurately predict the expected scatter profiles from these materials. The convolution shown in Figures 17 and 18 was visually chosen to match the blurring observed in the first peaks of the two materials. Note, that these are shown with the *same* blurring kernel. The convolved and measure spectra differ more significantly at higher angle, due to the change in the angle of incidence to the detector, and other detector related efficiencies. It was not possible to completely characterize these as it would have required a angular measurement that was not possible with out detector geometry

## 11. Experiments with Breast Specimens

We have tested the imaging system using breast biopsy specimens. These specimens were obtained after IRB review as an exempt study, under expedited review. The specimens were anonymous when provided to us. An example of six such specimens is shown in Figure 6. The specimens are held in a plastic cassette, and set in wax. We were not able to identify the scattering signature of calcium hydroxyapatite or calcium oxylate with any specimen.

Based upon the results in Sections 9 and 10, we can estimate the minimum size calcification that would be readily detectable. Using a technique of 49 kVp, 200 mAs would result in minimum detectable calcification size of 250 microns for calcium hydroxyapatite and 350 microns for calcium oxylate. The resulting dose to a 4 cm thick breast (composition 50% glandular/ 50% adipose) would be 14.8 mGy. Note that this dose is given for reference purposes only, as we showed above that 4 cm of tissue would completely obscure the scattering signature of any calcification. Clearly this technique is not clinically practical as an *in vivo* test; however, it may be that this technique has relevance in a pathology lab. One of the original motivations for this work was that microtomes used in histopathology often dislodge calcifications and eject them from the tissue specimen. The ability to image and identify calcification composition prior to sectioning the specimen may be of interest to pathologists.

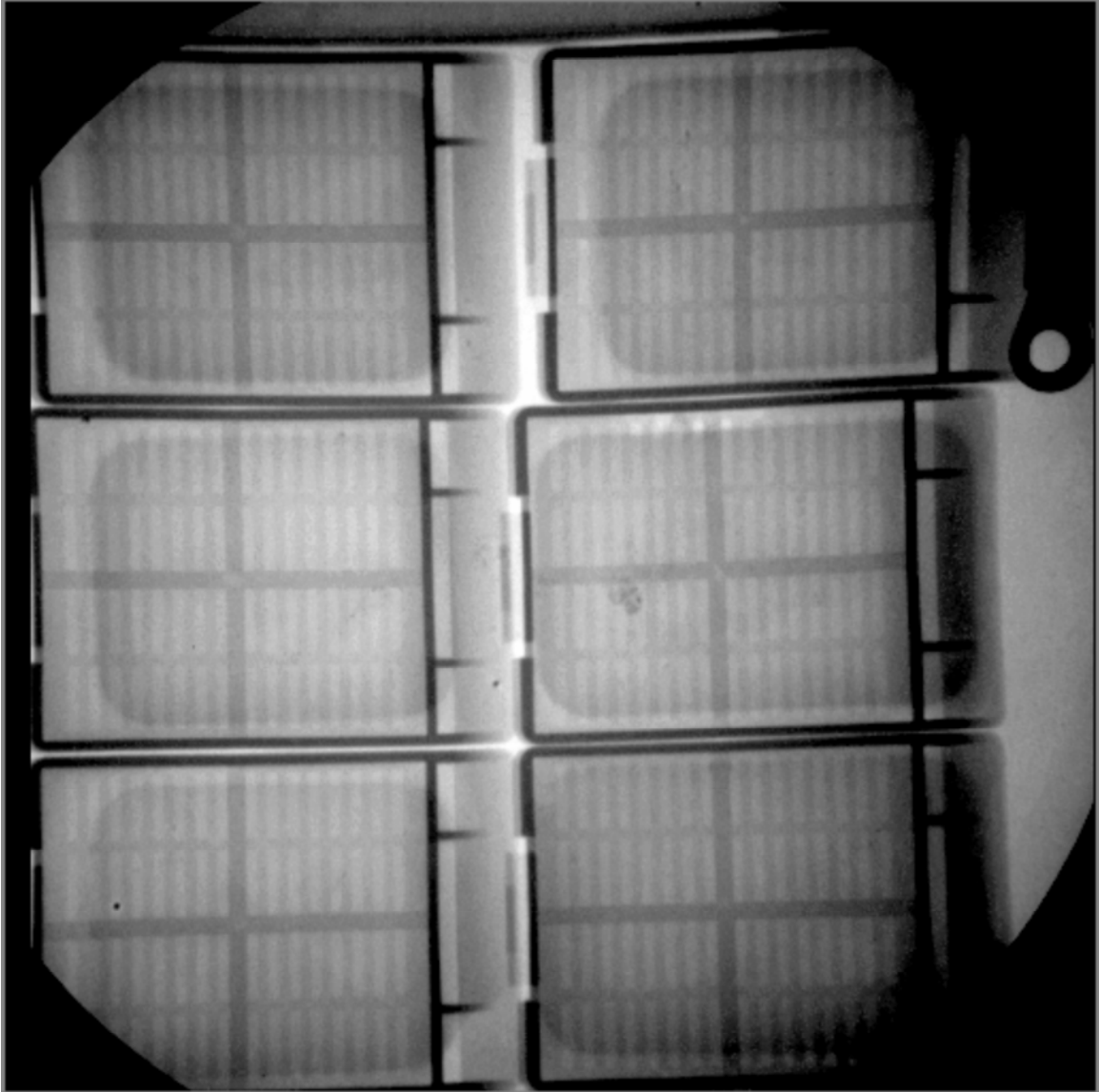


**Figure 20: Sample radiograph of 6 biopsy specimens, each held in a plastic cassette and set in wax. The middle cassette on the right column shows several large calcifications.**

## 12. X-ray Spectra Modeling

The coherent scatter modeling required that we model the x-ray spectrum in order to simulate our experimental conditions. In particular, we needed these data to determine the x-ray spectra and fluence rates. For spectra below 40 kV, we used the Boone model [6]. However, we simulated x-ray spectra in the range of 40 to 49 kV by extrapolating Boone's model. Boone parameterized spectra measured at the FDA for Mo, Rh and W target x-ray tubes operated between 18 and 40 kV. Each energy bin in the spectra was fitted in terms of the photon fluence as a function of kV using first, second order or third order polynomials. We believe that these data are over-fitted. This will become evident when we consider how to extrapolate the data.

In this report, we will concentrate on the extrapolation of the Rh target spectra. The extrapolation was split in two parts. Below 24 keV we used the parameters from Boone's paper for the extrapolated kVs. Above 24 keV, which we will refer to as the tails of the spectra, we refitted the spectra. In performing our fits, we assumed that: 1) for a given kV the photon fluence in the tails are linear with keV; 2) the slopes of the linear fits of the tails decrease with increasing kV; and 3) the photon fluence is zero at the maximum energy of each spectrum.

In Figure 21 we show spectra between 26 and 49 kV using Boone's parameters. Note that the shapes of the extrapolated spectra (grey) are similar to the published ones (black). Figure 21-b shows the low energy part in detail. The fluctuations in the extrapolated data are clearly artifactual. We have not addressed these artifacts as this low energy range is typically filtered from the beam. Next, consider the characteristic radiation peaks. Theoretically, for a thin target, the ratio of the  $K_{\alpha}$  to  $K_{\beta}$  peak is constant; for a Rh target this ratio is 5.46. The target of an x-ray tube is not thin, but to a first approximation we can consider it as thin because the electrons incident on the anode are much less penetrating than the fluorescent x-rays. Figure 22 shows that  $K_{\alpha}/K_{\beta}$  decreases starting at 38 kV. This decrease may be due to erroneous fitting. However, it could also be explained by beam hardening in the thick Rh target. This would be consistent with our data, as beam hardening would cause the fraction of  $K_{\beta}$  to increase. Figure 21-c is a detail of the tails. Again one can see the effect of over-fitting. We could have kept the tails as they are and extrapolated them beyond 40 keV. However, as this energy range is of significance in our experiments, we chose to refit them. Using the assumptions stated above, we calculated the slopes of the tails for the spectra from 34 to 40 kV. The slopes were calculated from 26.5 keV using linear interpolation. We applied a least squares fit and used this fit to estimate the slopes of the tails of the extrapolated spectra. Figure 21-c shows our fits. In analogy with Boone's model, the photon fluence were fitted as function of kV for each energy bin. We applied first, second and third order fits. We chose the simplest fit for each energy bin. The residuals between the fits and the data were 2 orders of magnitude smaller than the actual data.

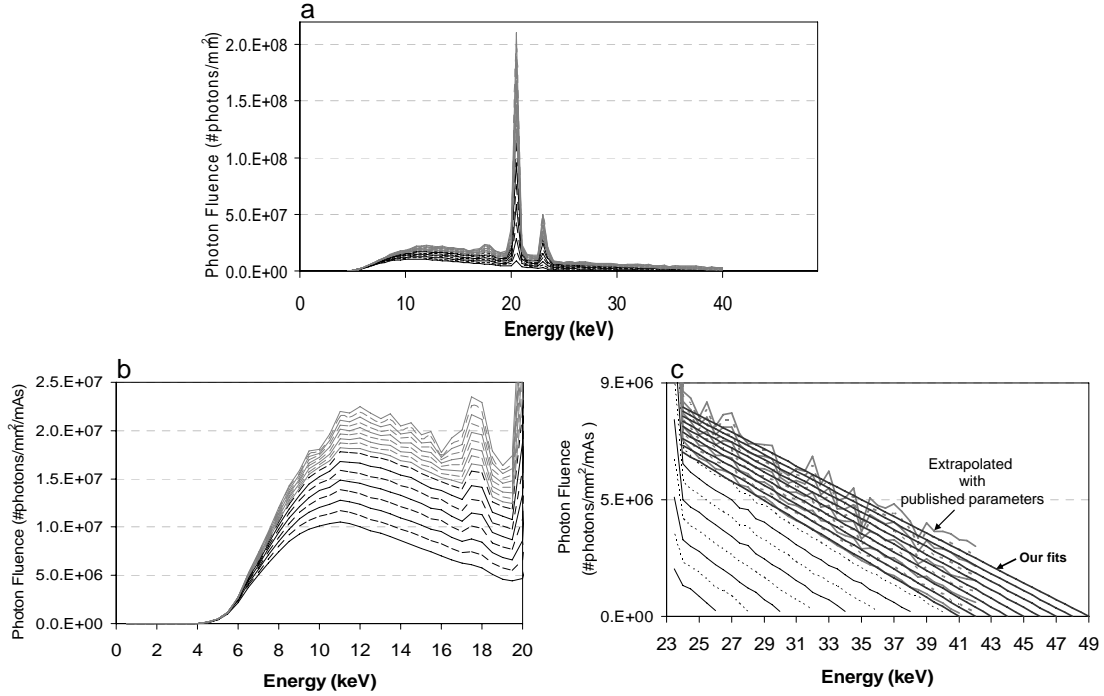
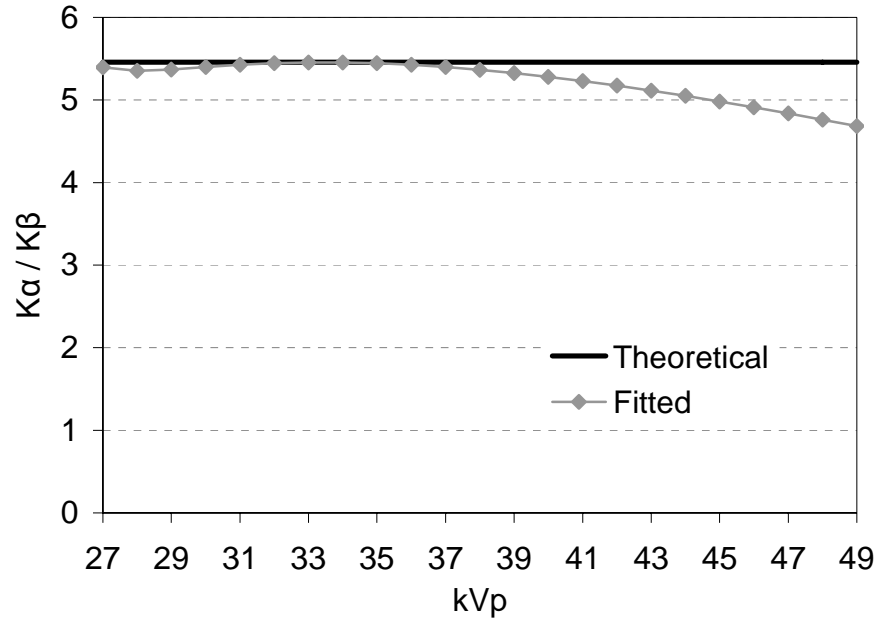


Figure 21: a) X-ray spectra from 26 kV to 49 kV using Boone’s parameters. Note that the extrapolated spectra (grey) have the same shape as the published spectra by Boone (black). b) Detail of the low-energy region of the spectra shown in a). Note that the fluctuations in the extrapolated spectra are artifactual. c) Detail of the tails of the spectra shown in a). These fluctuations are also artifactual.

We validated our simulations using a least-squares comparison (i.e., minimizing the  $\chi^2$  values) between measured and simulated attenuation data. We used Al filters (99.997 % pure, Alfa Aesar, Ward Hill, MA) to determine the attenuation curves. The minimum  $\chi^2$  was found by adjusting the kV ( $kV_{\text{equivalent}}$ ) and adding extra Al ( $Al_{\text{equivalent}}$ ) to the simulated spectra. We also compared the half value layers (HVL), quarter value layers (QVL), eight value layers (EVL) and tenth value layers (TVL) of the measurements and the simulations. The measurements were performed with a Senographe 2000D (GE Medical Systems, Milwaukee, WI). The Senographe 2000D was operated with a Rh target and 0.25 mm Rh or 0.27 mm Cu filtration. We used the Cu filter to emphasize the tails. The tube has a 0.69 mm thick Be window; a 2 mm thick compression paddle was in the x-ray beam; the distance from the target to the exposure meter was 43 cm.

We modeled this system by filtering our fitted Rh spectra with added filtration simulated to match the experimental setup. Tables 2 and 3 demonstrate that the extrapolation of Boone’s spectral models agree well with our measurements. Shown are the equivalent kV ( $kV_{\text{equivalent}}$ ) and equivalent Al filtration ( $Al_{\text{equivalent}}$ ) of the simulated spectra for a nominal kV that results in the smallest  $\chi^2$ . HVL and QVL are also presented for Rh and Cu filters; EVL and TVL are only presented for the Rh filter. The largest difference between the measured and simulated HVL, QVL, EVL and TVL is 1.8 % for the QVL at 49 kV with a Rh filter (48  $kV_{\text{equivalent}}$  and 0 mm  $Al_{\text{equivalent}}$ ). Figure 24 show examples of Rh spectra filtered with 0.27 mm Cu. The largest difference between the measured and simulated HVL and QVL is 1.3 % for the QVL at 34 kV (33.5  $kV_{\text{equivalent}}$  and 0 mm  $Al_{\text{equivalent}}$ ). This occurs in the range of energies fitted by Boone. In the extrapolated

range, the largest difference, 0.6 %, was found for the QVL at 49 kV (48.4 kV<sub>equivalent</sub> and 0 mm Al<sub>equivalent</sub>).



**Figure 22:**  $K_{\alpha}/K_{\beta}$  for a thin Rh target (theoretical) and as calculated in the fitted spectra. Note that  $K_{\alpha}/K_{\beta}$  decreases from 38 kV.

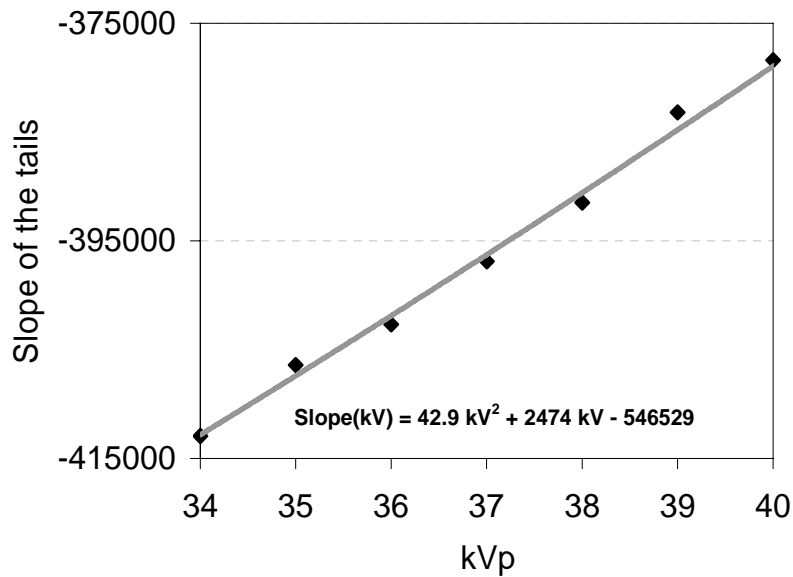


**Figure 23:** Slopes of the tails for the published spectra from 34 to 40 kV. A least squares fit was used to determine the slopes of the tails of the extrapolated spectra.

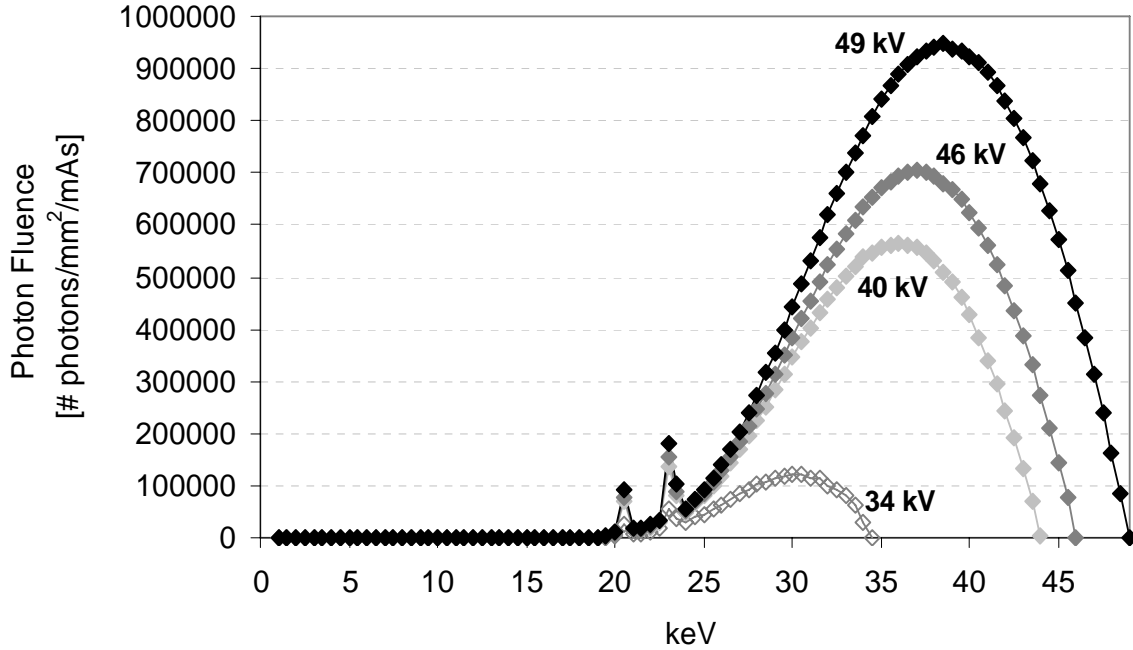


**Figure 24:** Examples of x-ray spectra from a Rh target filtered with 0.27 mm Cu. The fluence is specified 43 cm from the target.

Table 4 shows data from a GE DMR, acquired with a Mo-target x-ray source and 1 mm Al filtration. The x-ray tube window was composed of 0.69 mm thick Be and a 2 mm compression plate was again in place. Shown are  $kV_{\text{equivalent}}$  and  $Al_{\text{equivalent}}$  of the simulated spectra for a nominal kV that results in the smallest  $\chi^2$ . The measured and simulated estimates of the HVL and QVL are also presented. The simulated values are those that minimize the  $\chi^2$ . Again, the results in this table demonstrate that the extrapolation of the Boone's spectral models agree well with our measurements.

**Table 2:** Comparison of the measured and simulated attenuation data for a Rh target filtered with 0.25 mm Rh. HVL, QVL, EVL and TVL are expressed in mm Al.

Nominal kV	$kV_{\text{equivalent}}$	$Al_{\text{equivalent}}$	Measured				Simulated				
			HVL	QVL	EVL	TVL	HVL	QVL	EVL	TVL	X2
25	25.3	0.000	0.361	0.820	1.382	1.574	0.359	0.822	1.378	1.573	0.0001
28	28.4	0.000	0.412	0.949	1.589	1.818	0.411	0.950	1.593	1.819	0.0001
34	33.5	0.000	0.478	1.116	1.868	2.120	0.482	1.114	1.859	2.118	0.0001
40	39.8	0.000	0.556	1.244	2.088	2.382	0.546	1.258	2.092	2.384	0.0001
46	45.0	0.000	0.578	1.341	2.228	2.575	0.586	1.346	2.243	2.563	0.0005
49	48.0	0.000	0.612	1.365	2.309	2.625	0.605	1.390	2.325	2.662	0.0006

**Table 3.** Comparison of the measured and simulated attenuation data for a Rh-target tube filtered with 0.27 mm Cu.

Nominal kV	$kV_{\text{equivalent}}$	$Al_{\text{equivalent}}$	Measured		Simulated		$\chi^2$
			HVL	QVL	HVL	QVL	
34	33.5	0.0	1.711	3.532	1.713	3.579	0.00009
40	39.4	0.0	2.232	4.750	2.238	4.738	0.00012
46	45.5	0.0	2.779	5.978	2.787	5.978	0.00005
49	48.4	0.0	3.060	6.619	3.063	6.578	0.00006

**Table 4.** Comparison of the measured and simulated attenuation data for a Mo-target tube filtered with 1 mm Al.

nominal kV	kV <sub>equivalent</sub>	Al <sub>equivalent</sub>	Measured		Simulated		$\chi^2$
			HVL	QVL	HVL	QVL	
22	21.1	0.075	0.388	1.285	0.385	1.286	0.00007
28	28.0	0.100	0.538	1.844	0.540	1.841	0.00005
34	35.0	0.050	0.607	2.050	0.609	2.197	0.00009
40	39.4	0.100	0.654	2.420	0.649	2.442	0.00070
46	45.4	0.150	0.698	2.734	0.686	2.736	0.00071
49	49.0	0.175	0.739	2.907	0.703	2.911	0.00422

We originally had planned on publishing these extrapolated data in the peer-reviewed literature. These data have been widely used since we first published them 2 years ago. However, based upon our these results, we were approached by the FDA (Kyle Myers, Private Communication) to assist them in fitting newly measured spectra that cover the range to 50 kV. This work is described in detail in the next section

## 13. X-ray spectral fitting

### 13.1. Data

Mo, Rh, and W-target spectra between 20 *kVp* and 50 *kVp* were measured at the Center for Devices in Radiological Health (US FDA, Rockville, MD). Spectra were measured in two *kVp* intervals. The measured photon fluence were binned into 0.5 keV intervals. Figure 25 shows the measured photon fluence of the Rh spectra as a function of *keV* and *kVp*.

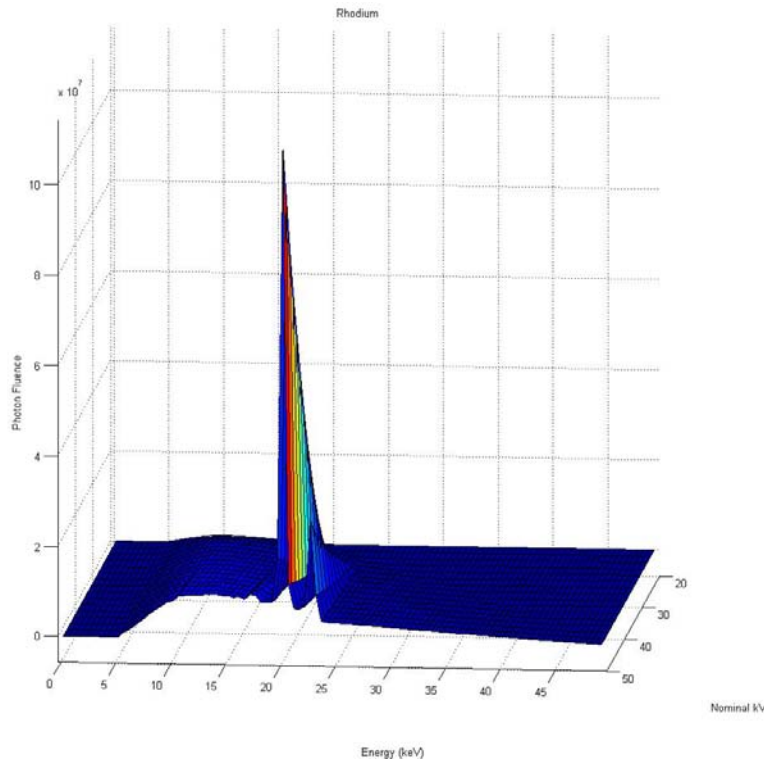


**Figure 25:** Measured Rh spectra as a function of *keV* and *kVp*.

## 14. Fitting energies up to 16.2 keV

For each experimentally obtained spectrum, the photon fluence in each energy bin was fitted versus  $keV$  using a least square fit:

$$photon\ fluence(kVp, keV) = A_{kVp_i} (keV - B_{kVp_i})(keV - C_{kVp_i})^2$$

where  $A_{kVp_i}$ ,  $B_{kVp_i}$  and  $C_{kVp_i}$  are fit parameters for each  $kVp_i$ , with  $i = 26$  to  $50$   $kVp$ .

Next,  $A_{kVp_i}$ ,  $B_{kVp_i}$  and  $C_{kVp_i}$  were fit versus  $kVp$ :

$$A_{kVp_i} = U_1 \cdot kVp_i^3 + U_2 \cdot kVp_i^2 + U_3 \cdot kVp_i + U_4$$

$$B_{kVp_i} = U_5 \cdot kVp_i + U_6$$

$$C_{kVp_i} = U_7 \cdot kVp_i^3 + U_8 \cdot kVp_i^2 + U_9 \cdot kVp_i + U_{10}$$

Figure 26 shows the values of  $A_{kVp_i}$ ,  $B_{kVp_i}$  and  $C_{kVp_i}$  as a function of  $kVp$  and their fits.

This figures shows that  $B_{kVp_i}$  and  $C_{kVp_i}$  can be satisfactorily fit using a second and third order polynomial,  $A_{kVp_i}$  varies “in steps” with  $kVp$ . Therefore, we modified our fit using:

$$photon\ fluence(kVp, keV) = A'_{kVp_i} (keV - B'_{kVp_i}) \left(1 - \frac{keV - B'_{kVp_i}}{C'_{kVp_i}}\right)^2$$

The transformations from the original fit to this new fit are:

$$A'_{kVp_i} = A_{kVp_i} \cdot (B_{kVp_i} - C_{kVp_i})^2$$

$$B'_{kVp_i} = B_{kVp_i}$$

$$C'_{kVp_i} = C_{kVp_i} - B_{kVp_i}$$

$A'_{kVp_i}$ ,  $B'_{kVp_i}$  and  $C'_{kVp_i}$  vary smoothly with  $kVp$  (Figure 27). Figure 28a shows a surface fit through the low energy part of the spectra using the 10 parameters that were derived above. Figure 28b is a profile through the 3D fit (photon fluence versus  $keV$  at  $30$   $kVp$ ); this figure shows that the experimental photon fluence data and the fit match well. The fit and the experimental spectra differed up to 7%.

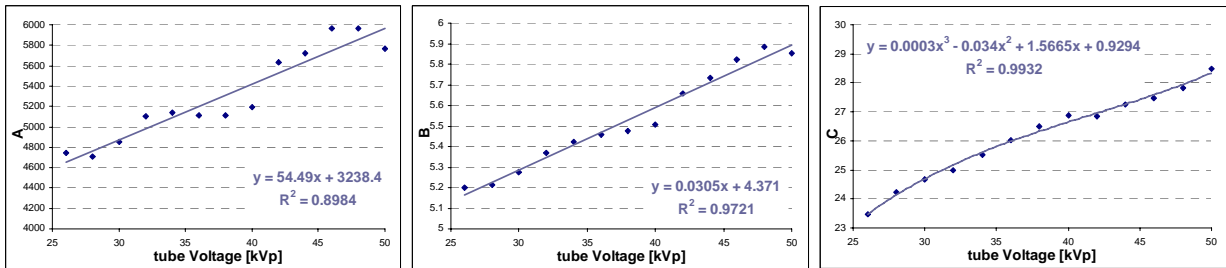


Figure 26:  $A_{kVp_i}$ ,  $B_{kVp_i}$  and  $C_{kVp_i}$  values versus  $kVp$  (solid diamonds) and their fits (solid lines) as a function of  $kVp$ .

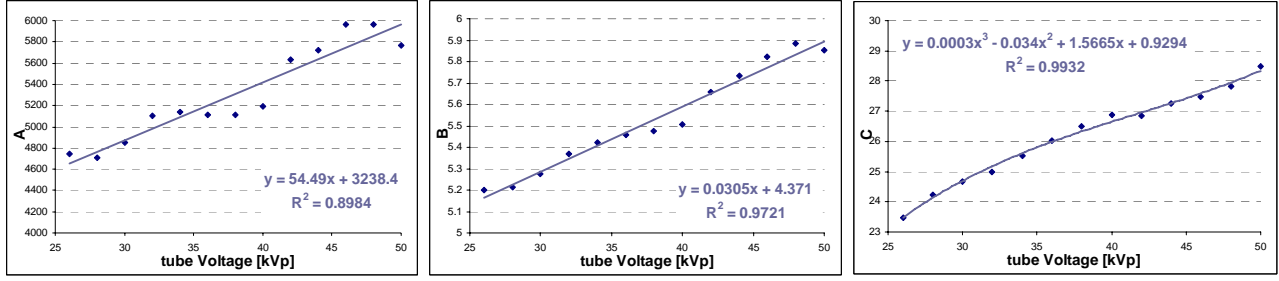


Figure 27: Modified fit parameters  $A'_{kVp_i}$ ,  $B'_{kVp_i}$  and  $C'_{kVp_i}$  (solid diamonds) and their fits (solid lines) as a function of kVp.

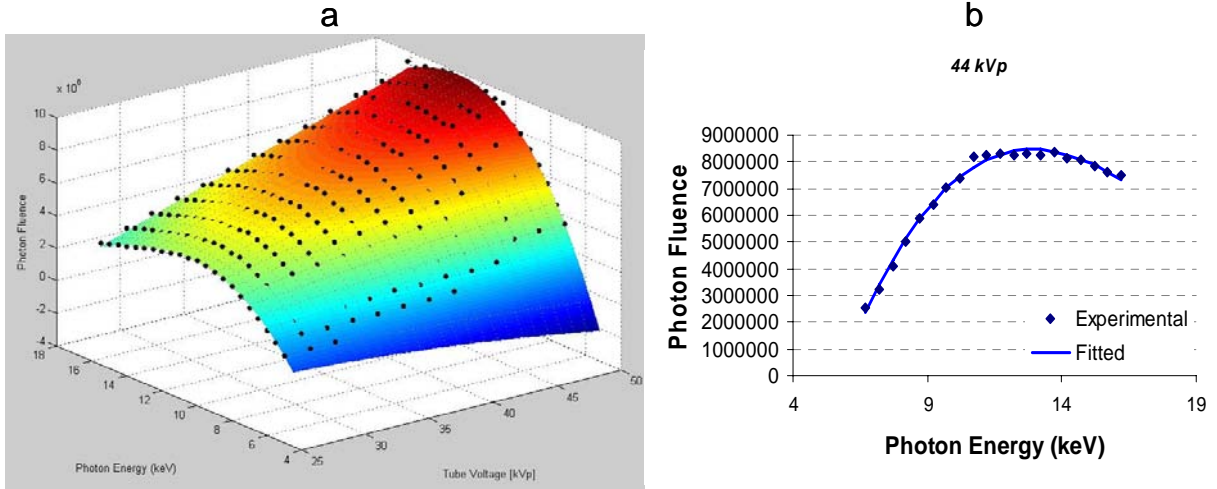


Figure 28: a. Photon fluence as a function of  $kVp$  and  $keV$ . The solid circles are experimentally obtained photon fluences, the surface plot is the fit using the 10 parameter model. b. is a profile through a. It shows the measured photon fluence (solid diamonds) and the fitted photon fluence (solid line) as a function of  $keV$  at 44  $kVp$ .

### 14.1. Fitting energies from 23.7 keV to kVp

In performing our fits in this energy regime, we assumed that: 1) for a given  $kVp$  the photon fluence in the tails are linear with  $keV$ ; 2) the slopes of the linear fits of the tails decrease with increasing  $kVp$ ; and 3) the photon fluence is zero at the maximum energy of each spectrum. Figure 29a shows the high energy part of the experimental spectra as a function of  $keV$  for tube voltages between 26  $kVp$  and 48  $kVp$ . This photon fluence as a function of  $keV$  was fit using first order polynomials (Figure 29a). Note that the slopes decreases as a function of  $kVp$ . Figure 29b shows the slopes from the linear fits as a function of  $kVp$ . The slopes as a function of  $kVp$  were fit using a third order polynomial. The 3D photon fluence; *i.e.* as a function of  $keV$  and  $kVp$ ; was plot as:

$$photon\ fluence(kVp, keV) = slope(kVp_i) \cdot (keV - keV_{0_i})$$

where  $keV_{0_i}$  is the  $keV$  where the photon fluence equals zero; in other words it equals  $kVp_i$ . Figure 30 shows a surface fit through the high energy part of the spectra using the parametric fit that was derived above.

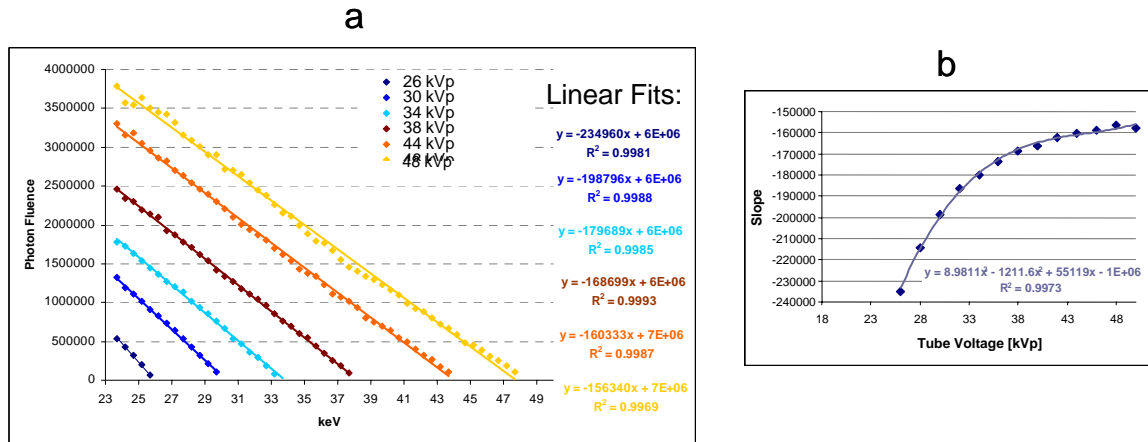


Figure 29: a. High energy part of the experimental spectra (solid diamonds) as a function of *keV* for various *kVps*. The solid lines are linear fits through the experimental data. b. Slopes from the linear fits in a. as a function of *kVp*.

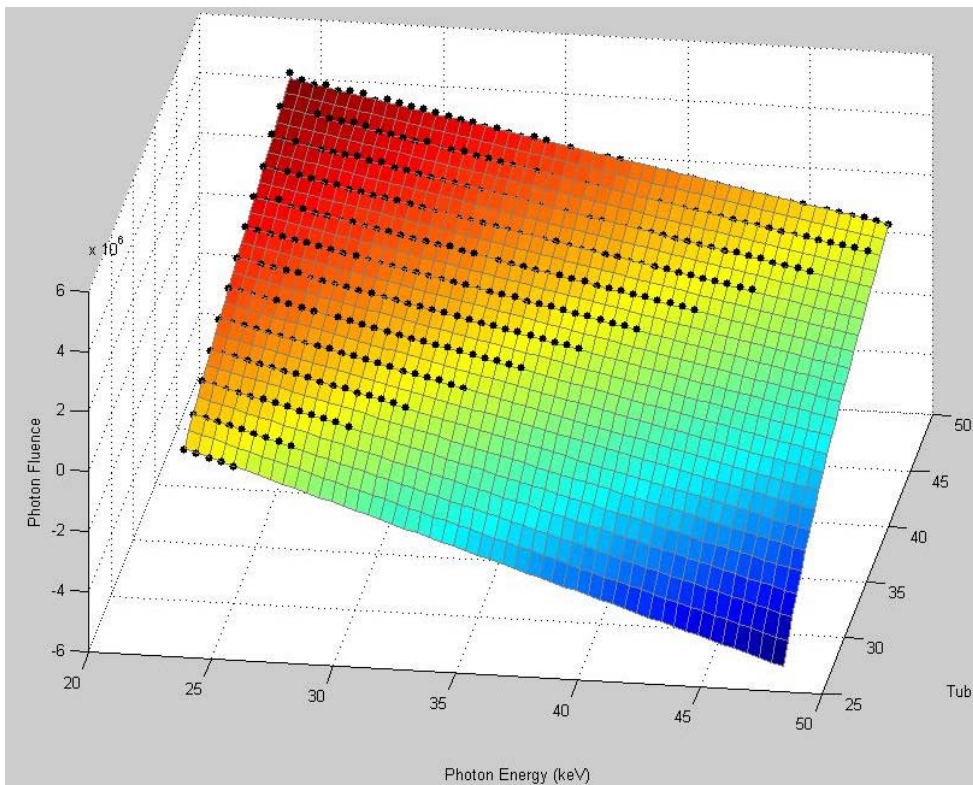


Figure 30: Photon fluence as a function of *kVp* and *keV*. The solid circles are experimentally obtained photon fluences, the surface plot is the fit using the model.

## 14.2. Fitting energies from 16.7 to 23.2 keV

For the mid energy regime, which includes the K-edges, we fitted, for each keV, the photon fluence as a function of kVp. It was impossible to fit this part of the spectra using

a 3D fit. Figure 31 shows some examples. The optimal fits were 1<sup>st</sup> order polynomials at all keVs except at 19.7 keV, 20.2 keV (K-edge of Rh), and 20.7 keV, 22.7 keV and 23.2 keV (K-edge of Rh) where a 2<sup>nd</sup> order polynomial fit give the best results.

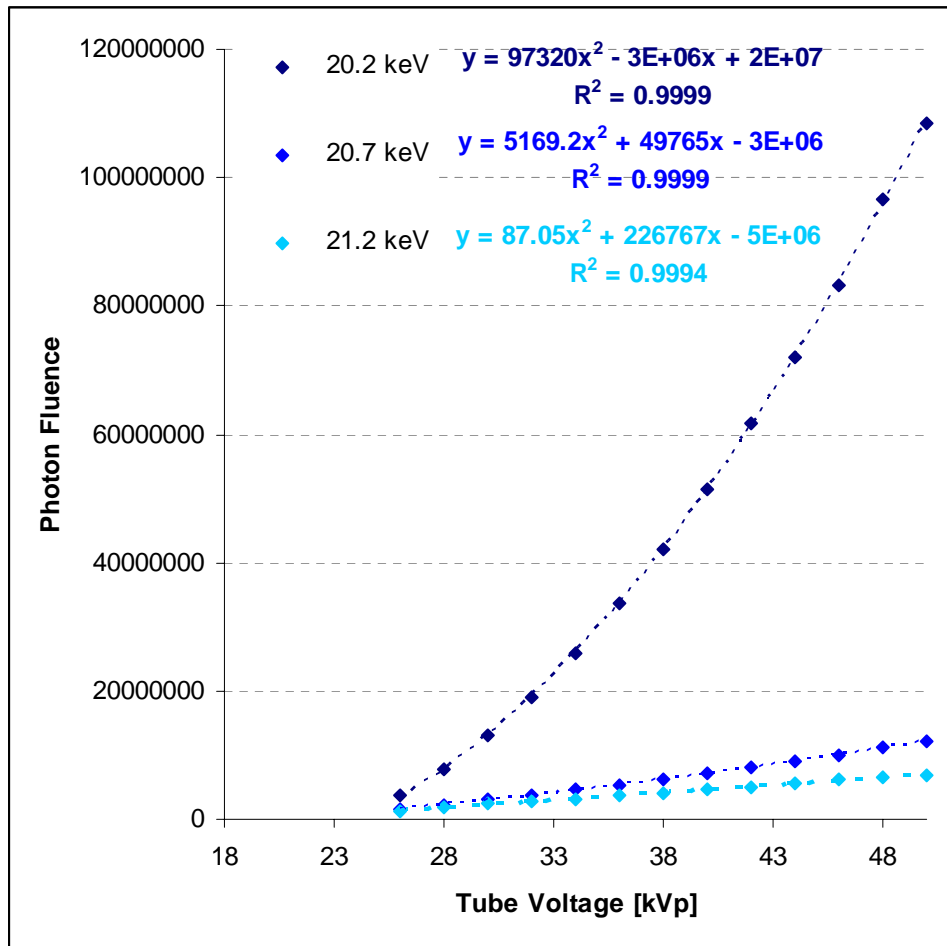


Figure 31: Photon fluence as a function of *kVp* for the energy bins 20.2, 20.7 and 21.2 keV.

### 14.3. Summary

At this time, we are continuing to work with the FDA on fitting these data, with the intention of publishing the data and fits towards the end of 2007. The data fitting has led the investigators at the FDA to question certain aspects of the data corrections applied to the measured spectra (so-called “stripping algorithms”). We are working with the FDA on these analyses and will then subsequently publish these data and the fits to the data.

It is important to understand the relevance of these results. Prior to our analysis, the most widely used spectral model for breast imaging was that of Boone [6]. Those data were severely overfit; a total of 84 fitting parameters were used. By carefully choosing a spectral model and fitting methodology, we have reduced this to a total of 17 parameters. We expect these data to become the industry standard for modeling mammography spectra when published.

## Key Research Accomplishments:

The following is a brief summary of key research accomplishments arising from this grant:

- We have designed and assembled a working x-ray diffraction imaging system using a pseudo-monochromatic x-ray beam.
- We have characterized the detector using known materials, and have used this characterization in the identification of calcific materials.
- We experimentally measures the diffraction spectra of calcific materials, and compared them to calculated values with considerable agreement
- We can predict the signal intensity as a function of mass of the calcification in the x-ray beam. Based on these calcifications, the minimum size detected is on the order of 0.25 to 0.35 mm diameter, in the absence of other scattering materials.
- The scattering signal from calcifications is lost when placed in anatomically appropriate breast thicknesses ( $> 2\text{cm}$ ), thus the method is likely to only have value *ex vivo*.
- To complete the modeling of our detector, we developed a validated extrapolation of Boone's spectral models. This extrapolation was presented at the SPIE Medical Imaging Conference in 2006, and has become widely cited and used. The model has application in a number of fields including contrast-enhanced mammography and tomosynthesis.
- Based on these results, we have formed a collaboration with the FDA to fit new x-ray spectral data. Our preliminary fit is described, and we are currently working with the FDA to complete this work for publication this year.

## Reportable Outcomes:

### Research Paper, Peer-Reviewed

1. Maidment ADA, Albert M, Kao YH. : Determination of Calcification Composition Proceedings of the 7th International Workshop on Digital Mammography. The University of North Carolina, Biomedical Research Imaging Center, Chapel Hill, NC (eds.). Page: 364-369, 2005.
2. Ann-Katherine Carton, Jingjing Li, Sara Chen, Emily Conant and Andrew D.A. Maidment: Optimization of Contrast-Enhanced Digital Breast Tomosynthesis. 8th International Workshop, IWDM 2006, Digital Mammography. Susan M. Astley et al (eds.). Springer, Page: 183-189, June 2006.

### Research Papers, Non-peer Reviewed

1. Maidment ADA and Albert M. "Tissue Discrimination Methods in Mammography". In: Advances in Digital Radiography: RSNA Categorical Course in Diagnostic Radiology Physics 2003. Radiological Society of North America, Oak Brook, IL, 2003. (and CD-ROM)
2. Carton, AK, Li J, Albert M, Chen S, and Maidment ADA. "Quantification for Contrast Enhanced Digital Breast Tomosynthesis," Physics of Medical Imaging: Proc. SPIE 6142, edited by E.L. Siegel, E.A. Krupinski, and M. Sonka (2006).

### Abstracts:

1. Maidment ADA and Albert M. A Novel Method for the Determination of Calcification Composition. The Department of Defense Breast Cancer Research Program Meeting – Era of Hope Proceedings. Volume II, p. 30-8, September 2002.
2. Boone JM, Carson P, Cherry S, Giger ME, Hendrick RE, Lewin J, Maidment ADA, and Niklason LT. "New Advances in Breast Imaging", Medical Physics, **30**(6), 1391 (2003).
3. Maidment ADA. "Tissue Discrimination Methods in Mammography" (abstr.), In: Radiological Society of North America scientific assembly and annual meeting program. Oak Brook, IL, 35-6 (2003).
4. Maidment ADA, Albert M, and Kao YH, "Determination of Calcification Composition by Coherent Scatter Imaging". Program of the 7<sup>th</sup> International Workshop on Digital Mammography, June 2004.
5. Maidment ADA. "Nine Orders of Magnitude: Imaging from Man to Molecules", Medical Physics, **31**(6), 1741-2 (2004).
6. Maidment ADA. "Tissue Discrimination Methods in Mammography" (abstr.), In: Radiological Society of North America scientific assembly and annual meeting program. Oak Brook, IL, 123 (2004).

7. Maidment ADA. "Tissue Discrimination Methods in Mammography" (abstr.), In: Radiological Society of North America scientific assembly and annual meeting program. Oak Brook, IL, (2005).
8. Carton AK, Chen SC, Albert M, Conant EF, Schnall MD, and Maidment ADA. Technical Development of contrast-enhanced Digital Breast Tomosynthesis. (abstr.), In: Radiological Society of North America scientific assembly and annual meeting program. Oak Brook, IL, (2005).
9. Maidment ADA and Kao YH. Characterization of Breast Calcifications using X-ray Diffraction. *Medical Physics* **33**(6), 2251, (2006).

#### **Invited Lectures:**

1. Boone JM, Carson P, Cherry S, Giger ME, Hendrick RE, Lewin J, Maidment ADA, and Niklason ET. "New Advances in Breast Imaging", 45<sup>th</sup> Annual Meeting of the American Association of Physicists in Medicine, San Diego, CA, August 12, 2003.
2. Maidment ADA. "Tissue Discrimination Methods in Mammography". 89th Scientific Assembly of the Radiological Society of North America, Chicago, IL, Dec. 4, 2003.
3. Maidment ADA. "Looking towards the Future of Mammographic Imaging". Royal Marsden Hospital, London, England, April 5, 2004.
4. Maidment ADA. "Looking towards the Future of Mammographic Imaging". General Electric Medical Systems, Buc, France, April 26, 2004.
5. Maidment ADA. "Nine Orders of Magnitude: Imaging from Man to Molecules", 46<sup>th</sup> Annual Meeting of the American Association of Physicists in Medicine, Pittsburgh, PA, July 26, 2004. (President's Symposium)
6. Maidment ADA. "Tissue Discrimination Methods in Mammography". 90th Scientific Assembly of the Radiological Society of North America, Chicago, IL, Dec. 2, 2004.
7. Maidment ADA. "Nine Orders of Magnitude: Imaging from Man to Molecules", SPIE Medical Imaging 2004, California, February 14, 2005. (Plenary Speaker)
8. Maidment ADA. "Thoughts on the Future of Radiology", Grand Rounds, University of California San Diego, Department of Radiology, San Diego, CA, February 15, 2005.
9. Maidment ADA. "Nine Orders of Magnitude: Imaging from Man to Molecules", Suntharalingam Lecture, Thomas Jefferson University, Department of Radiation Oncology, March 2, 2005.

10. Maidment ADA. "Radiology – Fusing Form and Function", Grand Rounds, MD Anderson Cancer Center, Department of Medical Physics, Houston, TX, March 8, 2005.
11. Maidment ADA. "Nine Orders of Magnitude: Imaging from Man to Molecules", Conference of Radiation Control Program Directors, Kansas City, KS, April 26, 2005.
12. Maidment ADA. "Nine Orders of Magnitude: Imaging from Man to Molecules", Metropolitan Washington DC Computer-Assisted Surgery Society (WASHCAS), National Library of Medicine, Bethesda, MD, March 15, 2005.
13. Maidment ADA. "Tissue Discrimination Methods in Mammography". 91st Scientific Assembly of the Radiological Society of North America, Chicago, IL, Nov. 27, 2005.
14. Maidment ADA. "Fusing Form and Function: The evolution of Radiology". Swedish Society for Automated Image Analysis. Umea, Sweden, March 16, 2006
15. Maidment ADA. "The Scale of Medical Imaging". Computer Applications in Radiology and Surgery Conference. Osaka, Japan, June 2006.

#### **Proffered Presentations and Posters:**

1. Maidment ADA and Albert M. A Novel Method for the Determination of Calcification Composition. The Department of Defense Breast Cancer Research Program Meeting – Era of Hope, Orlando, FL, September 25-28, 2002.
2. Carton AK, Chen SC, Albert M, Conant EF, Schnall MD, and Maidment ADA. Technical Development of contrast-enhanced Digital Breast Tomosynthesis. 91st Scientific Assembly of the Radiological Society of North America, Chicago, IL, December 2, 2005.
3. Carton, AK, Li J, Albert M, Chen S, and Maidment ADA. "Quantification for Contrast Enhanced Digital Breast Tomosynthesis," SPIE Medical Imaging 2005 (Physics of Medical Imaging) San Diego, California, February 12, 2006.
4. Carton AK, Li J, Chen S, Conant EF, and Maidment ADA. "Optimization of Contrast-Enhanced Digital Breast Tomosynthesis". 8<sup>th</sup> International Workshop, IWDM 2006", Manchester, UK, June 19, 2006.
5. Maidment ADA and Kao YH. Characterization of Breast Calcifications using X-ray Diffraction. 48<sup>th</sup> Annual Meeting of the American Association of Physicists in Medicine, Orlando, FL, August 2, 2006.

## Conclusions:

We have developed a technique that can determine the composition of calcific materials using x-ray coherent scatter. In the process, we developed a bench-top coherent scatter imaging system. Acquired images are processed via various normalizations; radial averaging is applied to produce scatter spectra. We have demonstrated that the coherent scatter spectra are unique and readily distinguishable for the three main breast calcification compositions (namely, calcium hydroxyapatite, calcium oxalate monohydrate, and calcium oxalate dihydrate) in reagent form. We have developed an analytical formulation to predict the signal from calcifications, and we have successfully modeled the imaging system.

The original intent for the system was to image calcifications *in vivo* prior to biopsy, thereby potentially allowing one to avoid biopsy on Type I calcifications which are known to be exclusively associated with benign disease. Our experiments indicate that this is not possible. The amount of scatter from normal breast tissues dwarfs the scatter from the calcifications. As a result, the method is, at best, of value only for *ex vivo* measurements. We intend to pursue this use of this technology in histopathological examination of tissue.

In conclusion we have successfully been able to measure diffraction spectra of calcified materials, and have shown that the diffraction spectra of calcium hydroxyapatite, whewellite and weddellite are sufficiently different to allow discrimination of the materials by diffraction. However, the scattering signature is not sufficiently large to allow the method to be used *in vivo*.

## References:

---

- 1 L. W.-Levy and J. Lanipece. Sur la formation des hydrates de l'oxalate de calcium. Comptes Rendus Hebdomadaires Des Seances de L'Academie Des Sciences, 1962, v. 254, p. 296--298.
- 2 B. Tomazic and G. H. Nancollas. Crystal Growth of Calcium Oxalate Hydrates: A Comparative Kinetics Study, Journal of Colloid and Interface. Science, v. 75, no. 1, 1980, p. 149-160
3. Batchelar DL, Chun SS, Wollin TA, Tan JK, Beiko DT, Cunningham IA, et al. Predicting urinary stone composition using X-ray coherent scatter: a novel technique with potential clinical applications. Journal of Urology. 2002;168(1):260-5.
4. Batchelar DL, Cunningham IA. Material-specific analysis using coherent-scatter imaging. Medical Physics. 2002;29(8):1651-60.
5. Westmore MS, Fenster A, Cunningham IA. Angular-dependent coherent scatter measured with a diagnostic x-ray image intensifier-based imaging system. Medical Physics. 1996;23(5):723-33.
6. Boone JM, Fewell TR, Jennings RJ. Molybdenum, rhodium, and tungsten anode spectral models using interpolating polynomials with application to mammography. Medical Physics. 1997;24(12):1863-74.

## **Appendices:**

None.